Computational Mechanics
https://doi.org/10.1007/s00466-024-02533-w

ORIGINAL PAPER

Deformation twinning as a displacive transformation: computational aspects of the phase-field model coupled with crystal plasticity

Przemysław Sadowski[1] · **Mohsen Rezaee-Hajidehi**[1] · **Stanisław Stupkiewicz**[1]

Received: 1 February 2024 / Accepted: 30 July 2024

Abstract
Spatially-resolved modeling of deformation twinning and its interaction with plastic slip is achieved by coupling the phase-field method and crystal plasticity theory. The intricate constitutive relations arising from this coupling render the resulting computational model prone to inefficiencies and lack of robustness. Accordingly, together with the inherent limitations of the phase-field method, these factors may impede the broad applicability of the model. In this paper, our recent phase-field model of coupled twinning and crystal plasticity is the subject of study. We delve into the incremental formulation and computational treatment of the model and run a thorough investigation into its computational performance. We focus specifically on evaluating the efficiency of the finite-element discretization employing various element types, and we examine the impact of mesh density. Since the micromorphic regularization is an important part of the finite-element implementation, the effect of the micromorphic regularization parameter is also studied.

Keywords Deformation twinning · Microstructure · Phase-field method · Crystal plasticity · Finite element method

1 Introduction

The phase-field method is an effective computational approach that has been actively used in the last few decades to model and study the microstructure evolution in various material processes. These include, but are not limited to, solidification and grain growth [e.g., 1–5], displacive phase transformation [e.g., 6–9] and ferroelectric/ferromagnetic phase separation [e.g., 10–13], see also the recent review [14]. The strength of the phase-field method lies in its ability to model complex microstructural patterns without the explicit tracking of the microstructural interfaces. In the context of the Allen–Cahn-type phase-field models, each material phase is characterized by a non-conserved order parameter which typically represents the phase volume fraction. The evolution of the order parameters, and thus the evolution of the material interfaces, is then described by the time-dependent Ginzburg–Landau equation which drives the system towards an energy-minimizing configuration [15].

On the computational side, the phase-field method necessitates the use of a reasonably fine computational grid in order to properly resolve the diffuse interfaces and describe the interfacial energy effects, and thereby, to effectively capture the subtle microstructural features. This computational demand, which is more severe in the finite-element analysis rather than in the FFT-based analysis, has often limited the applications of the phase-field models to small computational domains or excessively diffuse microstructures. In response to this limitation, efforts have been directed towards developing more advanced phase-field models that retain accuracy while being computationally less restrictive, such as the sharp phase-field method [16, 17], length-scale-insensitive phase-field formulation [18], and the hybrid diffuse–semisharp

We dedicate this paper to Professor Jörg Schröder on the occasion of his 60th birthday, with which we would like to honour his notable contributions to the mechanics community. The numerous scientific achievements of Jörg Schröder include those related to refined constitutive modelling of complex materials and to development of efficient finite-element formulations for variety of problems. Both aspects are addressed in our work on phase-field modelling of deformation twinning and crystal plasticity.

✉ Stanisław Stupkiewicz
sstupkie@ippt.pan.pl

Przemysław Sadowski
psad@ippt.pan.pl

Mohsen Rezaee-Hajidehi
mrezaee@ippt.pan.pl

[1] Institute of Fundamental Technological Research (IPPT), Polish Academy of Sciences, Pawińskiego 5B, 02-106 Warsaw, Poland

Published online: 23 August 2024

approach [19], and also towards developing computational frameworks that enable large-scale simulations [20–22].

On the other hand, the incorporation of various physical mechanisms responsible for microstructural changes into the computational model can be achieved via integrating the phase-field method with other theoretical approaches. The combination of the phase-field method and crystal plasticity theory constitutes a class of multi-physics models that are intended to describe coupled micromechanical processes such as deformation twinning and dislocation slip [23–25]. From the computational standpoint, the strong coupling between the inelastic mechanisms introduces additional complexities to the constitutive equations. Therefore, to ensure the feasibility of the devised models, it is of particular importance to assess the computational performance and strive for optimal efficiency. This is the subject of the present work.

A finite-element-based phase-field model of coupled twinning and crystal plasticity has been developed in our previous work [26], which is specifically tailored to magnesium with an HCP crystal structure. The formulation of the model is based on the finite-deformation theory with a stretch-based kinematics of the deformation twinning and its constitutive relations assume a viscous evolution with a finite rate-independent threshold on the thermodynamic driving forces. The structure of the model follows the variational principle and its finite-element implementation leverages the augmented Lagrangian treatment of the mixed-type (viscous and rate-independent) evolution laws and the micromorphic regularization. The latter allows to restructure the model into a global–local problem and thus significantly facilitates the finite-element implementation.

The theoretical foundation of the model has been extensively discussed in [26] and the capability of the model in capturing the essential features of the twin microstructures has been demonstrated. However, limited attention has been devoted to the incremental formulation of the model and to its finite-element treatment. In the present paper, the related aspects are discussed in detail.

Secondly, we thoroughly examine the performance of the resulting computational model. We focus particularly on the efficiency and accuracy of the finite-element discretization employing different element types and on the impact of mesh density on the simulation results. To our knowledge, these aspects have not been systematically investigated in the framework of phase-field models coupled with crystal plasticity. In fact, even in the broader context of standard phase-field modeling, the related aspects are seldom explored, see [27]. At the same time, special attention has been given to the proper averaging of the material properties and to the calculation of the mechanical fields within the diffuse interfaces [28–32].

A notable feature of our implementation is the use of the penalty method for the micromorphic regularization, rather than the Lagrange-multiplier method, as adopted in [33]. As such, we also examine the effect of the micromorphic regularization parameter on the computational performance and simulation results.

Our simulations employ a setup of four differently-oriented grains. This setup, though relatively simple, enables us to capture effectively the twin nucleation, twin transmission through the grain boundaries, and most importantly, the complex interaction between twinning and plastic slip. Hence, it is considered as a reasonably sophisticated representative example to test the computational performance in different settings.

The paper is organized as follows. It begins with the presentation of the model in Sect. 2. In Sect. 3, the incremental formulation of the model is discussed in detail, followed by its computational treatment and finite-element implementation. Finally, the results of a comprehensive computational study are presented and discussed in Sect. 4.

2 Phase-field model of deformation twinning and crystal plasticity

In this section, the recently-developed finite-strain phase-field model of coupled twinning and crystal plasticity is briefly presented as a basis for the subsequent discussion of its incremental formulation and finite-element treatment in Sect. 3. For a more detailed background, argument and discussion, the reader is referred to [26].

2.1 Preliminaries

In the finite-deformation framework adopted in this work, the basic kinematic quantity is the deformation gradient, $\mathbf{F} = \nabla\boldsymbol{\varphi}$, defined as the gradient (taken in the reference configuration) of the deformation mapping $\boldsymbol{\varphi}$ that takes a material point from the reference configuration to the current configuration. The deformation gradient $\mathbf{F}$ is multiplicatively decomposed into its elastic part $\mathbf{F}_\mathrm{e}$ and inelastic part $\mathbf{F}_\mathrm{in}$,

$$\mathbf{F} = \mathbf{F}_\mathrm{e}\mathbf{F}_\mathrm{in}. \tag{1}$$

In the present context, the inelastic deformation described by $\mathbf{F}_\mathrm{in}$ may result from deformation twinning and from plastic slip in both the matrix and the twin, as detailed later. Prior to the onset of twinning, plastic slip in the matrix is the only mechanism of inelastic deformation, thus $\mathbf{F}_\mathrm{in} = \mathbf{F}_\mathrm{m}$, where $\mathbf{F}_\mathrm{m}$ results from the plastic deformation in the matrix and is governed by the classical flow rule of crystal plasticity (collective action of plastic slip on crystallographic slip systems in the matrix). If the twin boundary is treated as a sharp (zero-thickness) interface, then a material point experiences a strain jump as the twin boundary passes through it. Let

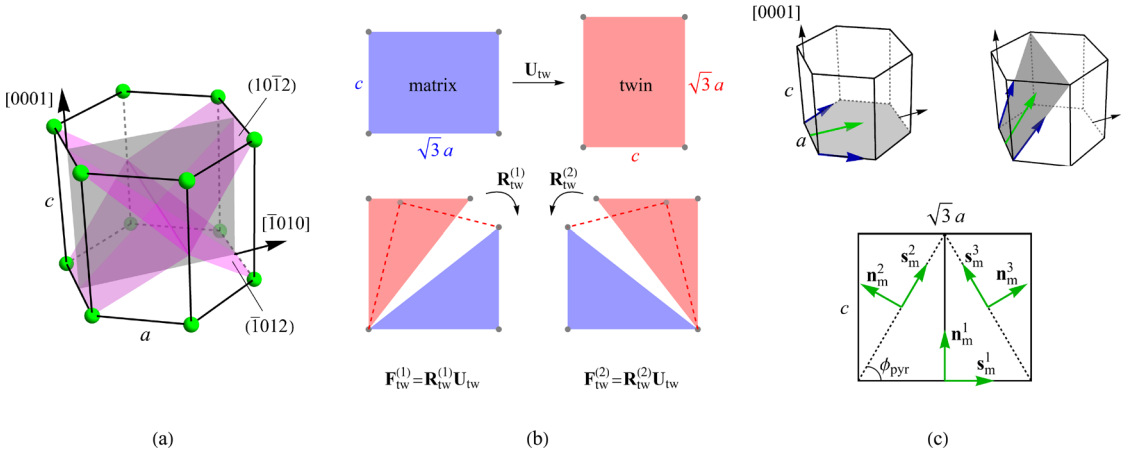

Fig. 1 Scheme of the $\{10\bar{1}2\}\langle\bar{1}011\rangle$ tensile twinning in HCP crystal structure of magnesium. **a** The $(10\bar{1}2)$ and $(\bar{1}012)$ twin planes of two conjugate twinning systems within the hexagonal unit cell. **b** Deformation twinning modeled as a displacive transformation involving the stretch $\mathbf{U}_{\rm tw}$ of the matrix lattice followed by a rigid-body rotation $\mathbf{R}^{(i)}_{\rm tw}$. **c** Three equivalent slip systems (one basal and two pyramidal) within the $(\bar{1}2\bar{1}0)$ plane. For more details, see [26]

us denote the corresponding deformation gradient by $\mathbf{F}_{\rm tw}$. Subsequently, this material point belongs to the twin (the product phase of the twinning transformation), and further inelastic deformation results from the plastic deformation in the twin. This deformation is described by the respective deformation gradient $\mathbf{F}_{\rm p}$ that is governed by the classical flow rule of crystal plasticity, however, the slip systems are those of the twin that are different from those of the matrix. The inelastic deformation gradient takes then the following form: $\mathbf{F}_{\rm in} = \mathbf{F}_{\rm p}\mathbf{F}_{\rm tw}\mathbf{F}_{\rm m}$, where $\mathbf{F}_{\rm tw}\mathbf{F}_{\rm m}$ is a fixed prior deformation ($\dot{\mathbf{F}}_{\rm m} = \mathbf{0}$, $\dot{\mathbf{F}}_{\rm tw} = \mathbf{0}$) and only $\mathbf{F}_{\rm p}$ evolves.

2.2 Stretch-based kinematics of deformation twinning

Twinning is a deformation mechanism that is conventionally described by simple shear on specific crystallographic twinning systems. In most cases, in particular in HCP, FCC and BCC crystals, twinning systems can be grouped into pairs of conjugate twinning systems that have the same shear plane and are crystallographically equivalent. Focusing on HCP crystals (although the reasoning applies equally to FCC and BCC crystals), let us consider one pair of conjugate twinning systems indexed by $i = 1, 2$. To fix attention, consider the $\{10\bar{1}2\}\langle\bar{1}011\rangle$ tensile twinning in magnesium and a pair of conjugate twinning systems with the $(10\bar{1}2)$ and $(\bar{1}012)$ twin planes, as illustrated in Fig. 1a.

Denoting by $\mathbf{m}^{(i)}$ and $\mathbf{a}^{(i)}$ the unit vectors that specify, respectively, the twin plane normal and the twinning shear direction ($\mathbf{m}^{(i)} \cdot \mathbf{a}^{(i)} = 0$), the deformation gradient describing the simple shear deformation associated with twinning takes the form

$$\mathbf{F}^{(i)}_{\rm tw} = \mathbf{I} + \gamma_{\rm tw}\mathbf{a}^{(i)} \otimes \mathbf{m}^{(i)}, \tag{2}$$

where $\gamma_{\rm tw}$ denotes the twinning shear [34],

$$\gamma_{\rm tw} = \frac{\alpha^2 - 1}{\alpha} = \frac{\sqrt{3}a}{c} - \frac{c}{\sqrt{3}a},$$
$$\alpha = \frac{\sqrt{3}a}{c} > 1, \tag{3}$$

with $c/a < \sqrt{3}$ for magnesium.

Polar decomposition of the deformation gradient $\mathbf{F}^{(i)}_{\rm tw}$ into a symmetric stretch tensor $\mathbf{U}^{(i)}_{\rm tw}$ and a rotation tensor $\mathbf{R}^{(i)}_{\rm tw}$ yields

$$\mathbf{F}^{(i)}_{\rm tw} = \mathbf{R}^{(i)}_{\rm tw}\mathbf{U}^{(i)}_{\rm tw}. \tag{4}$$

It can be checked that the stretch tensors of the conjugate twins are equal and that the rotation tensors are the inverse of each other, thus

$$\mathbf{U}^{(1)}_{\rm tw} = \mathbf{U}^{(2)}_{\rm tw} = \mathbf{U}_{\rm tw},$$
$$\mathbf{R}^{(1)}_{\rm tw} = \left(\mathbf{R}^{(2)}_{\rm tw}\right)^{\rm T} = \mathbf{R}_{\rm tw}. \tag{5}$$

Accordingly, we have

$$\mathbf{F}^{(1)}_{\rm tw} = \mathbf{R}_{\rm tw}\mathbf{U}_{\rm tw},$$
$$\mathbf{F}^{(2)}_{\rm tw} = \mathbf{R}^{\rm T}_{\rm tw}\mathbf{U}_{\rm tw}. \tag{6}$$

It follows that the two conjugate twinning systems, each characterized independently by a simple shear mechanism, can

be equivalently treated as a single deformation mechanism characterized by a volume preserving stretch $\mathbf{U}_{\rm tw}$. This formulation is particularly beneficial in the case of phase-field modeling of twinning since it leads to a reduced number of order parameters (3 instead of 6 in HCP, 6 instead of 12 in FCC and BCC) with an obvious reduction of the computational cost, considering that the order parameters are global unknowns. Note that, upon adopting the stretch-based kinematics of twinning, the rotation ($\mathbf{R}_{\rm tw}$ or $\mathbf{R}_{\rm tw}^{\rm T}$) which is needed to achieve compatibility between the matrix and the twin is naturally included in the elastic deformation gradient $\mathbf{F}_{\rm e}$ in Eq. (1) and becomes a part of the solution of the problem. It is stressed that the above stretch-based kinematics of twinning and the conventional shear-based kinematics are equivalent in the sharp-interface framework, but they are not fully equivalent in the diffuse-interface framework of the phase-field method, see the detailed discussion in [26]. While the conventional shear-based kinematics dominates in the literature, the stretch based kinematics has only a few applications, by Liu et al. [35] in a small-strain phase-field model of twinning and also more recently by Bruzy et al. [36] in a crystal-plasticity model of plastic slip and twinning.

2.3 Diffuse-interface kinematics of plastic slip and twinning

The presentation below is limited to the case of a single twin deformation variant that represents two crystallographic twinning systems, as discussed in Sect. 2.2. Concerning the kinematics, the extension to the general case of several twin variants is immediate, however, development and computer implementation of the corresponding complete phase-field model is more involved and will not be discussed here.

In the diffuse-interface framework of the phase-field method, a continuous order parameter η is introduced such that $\eta = 0$ represents the matrix, $\eta = 1$ represents the twin, $0 < \eta < 1$ represents a diffuse matrix–twin interface, and η satisfies the constraint $0 \le \eta \le 1$.

Consider first the case of twinning only. Within a diffuse interface, the inelastic deformation gradient $\mathbf{F}_{\rm in} = \mathbf{F}_{\rm tw}$ must be specified for the intermediate values of η between 0 and 1. Here, the following logarithmic mixing rule is adopted [9],

$$\mathbf{F}_{\rm tw}(\eta) = \exp(\eta \log \mathbf{U}_{\rm tw}), \quad \dot{\mathbf{F}}_{\rm tw}\mathbf{F}_{\rm tw}^{-1} = \dot{\eta} \log \mathbf{U}_{\rm tw}, \tag{7}$$

where the rate form $(7)_2$ results from the property of the tensor exponential: $\frac{\rm d}{{\rm d}t} \exp(t\mathbf{A}) = \mathbf{A} \exp(t\mathbf{A})$ for an arbitrary tensor $\mathbf{A}$. Note that the above mixing rule preserves the volume, i.e., $\det \mathbf{F}_{\rm tw} = \det \mathbf{U}_{\rm tw} = 1$ for $0 \le \eta \le 1$.

In the general case of twinning and plasticity, consistent with the logarithmic mixing rule (7), the following evolution law for $\mathbf{F}_{\rm in}$ is adopted [26],

$$\mathbf{L}_{\rm in} = \dot{\mathbf{F}}_{\rm in}\mathbf{F}_{\rm in}^{-1} = (1-\eta) \sum_{s=1}^{n_{\rm s}} \dot{\gamma}_{\rm m}^s \mathbf{s}_{\rm m}^s \otimes \mathbf{n}_{\rm m}^s + \eta \sum_{s=1}^{n_{\rm s}} \dot{\gamma}_{\rm p}^s \mathbf{s}_{\rm p}^s \otimes \mathbf{n}_{\rm p}^s + \dot{\eta} \log \mathbf{U}_{\rm tw}, \tag{8}$$

where the unit vectors $\mathbf{s}_{\rm m}^s$ and $\mathbf{n}_{\rm m}^s$ denote, respectively, the slip direction and slip plane normal of the slip system s in the matrix, $\dot{\gamma}_{\rm m}^s$ denotes the corresponding slip rate, and $n_{\rm s}$ is the number of slip systems. Likewise, $\mathbf{s}_{\rm p}^s$, $\mathbf{n}_{\rm p}^s$ and $\dot{\gamma}_{\rm p}^s$ denote the respective quantities in the twin (product). For $\eta = 0$ and $\dot{\eta} = 0$, Eq. (8) reduces to the classical flow rule of crystal plasticity in the matrix, and that for the twin is recovered for $\eta = 1$ and $\dot{\eta} = 0$.

The vectors specifying the slip systems in the twin ($\mathbf{s}_{\rm p}^s$, $\mathbf{n}_{\rm p}^s$) are related to those in the matrix ($\mathbf{s}_{\rm m}^s$, $\mathbf{n}_{\rm m}^s$) by a 180° rotation about vector $\mathbf{t}$ which is oriented at 45° with respect to the basal plane, namely $\mathbf{s}_{\rm p}^s = \mathbf{R}_{\rm m\to p}\mathbf{s}_{\rm m}^s$ and $\mathbf{n}_{\rm p}^s = \mathbf{R}_{\rm m\to p}\mathbf{n}_{\rm m}^s$, where $\mathbf{R}_{\rm m\to p} = 2\mathbf{t}\otimes\mathbf{t} - \mathbf{I}$. In the Cartesian coordinate system defined such that the x_1 and x_2 axes are oriented, respectively, along the $[\bar{1}010]$ and $[0001]$ crystallographic axes, the components of vector $\mathbf{t}$ are $\frac{\sqrt{2}}{2}(\pm 1, 1, 0)_{\rm C}$, see [26] for details.

2.4 Free energy and dissipation potential

The total (isothermal) free energy ψ comprises the elastic strain energy $\psi_{\rm e}$, the stored plastic energy $\psi_{\rm h}$, and the (interfacial) energy ψ_Γ of diffuse twin boundaries,

$$\psi(\mathbf{F}, \mathbf{F}_{\rm in}, \bar{\gamma}, \eta, \nabla\eta) = \psi_{\rm e}(\mathbf{F}_{\rm e}, \eta) + \psi_{\rm h}(\bar{\gamma}) + \psi_\Gamma(\eta, \nabla\eta) + I_{[0,1]}(\eta), \tag{9}$$

where $\mathbf{F}_{\rm e} = \mathbf{F}\mathbf{F}_{\rm in}^{-1}$, $\bar{\gamma}$ is the accumulated plastic slip,

$$\dot{\bar{\gamma}} = (1-\eta) \sum_{s=1}^{n_{\rm s}} |\dot{\gamma}_{\rm m}^s| + \eta \sum_{s=1}^{n_{\rm s}} |\dot{\gamma}_{\rm p}^s|, \tag{10}$$

and $I_{[0,1]}$ denotes the indicator function that imposes the bound constraint $0 \le \eta \le 1$.

The individual components of the total free energy are specified as follows. The elastic strain energy $\psi_{\rm e}$ is adopted as a quadratic function of the logarithmic elastic strain $\mathbf{H}_{\rm e}$ (Hencky-type energy),

$$\psi_{\rm e}(\mathbf{F}_{\rm e}, \eta) = \frac{1}{2}\mathbf{H}_{\rm e} \cdot \mathbb{L}(\eta)\mathbf{H}_{\rm e}, \quad \mathbf{H}_{\rm e} = \frac{1}{2}\log(\mathbf{C}_{\rm e}), \quad \mathbf{C}_{\rm e} = \mathbf{F}_{\rm e}^{\rm T}\mathbf{F}_{\rm e}, \tag{11}$$

where $\mathbb{L}(\eta) = (1-\eta)\mathbb{L}_{\rm m} + \eta\mathbb{L}_{\rm p}$ is the fourth-order elastic stiffness tensor. Here, $\mathbb{L}_{\rm m}$ and $\mathbb{L}_{\rm p}$ are the elastic stiffness

tensors of the matrix and twin, respectively, which are symmetry-related through the rotation $\mathbf{R}_{\mathrm{m}\to\mathrm{p}}$ (i.e., $\mathbb{L}_{\mathrm{p}} = \mathbf{R}_{\mathrm{m}\to\mathrm{p}} \circ \mathbb{L}_{\mathrm{m}}$). The Hencky-type strain energy is adopted here as a simple and general way to achieve a good behavior of the anisotropic elastic strain energy for a sufficiently large range of elastic strains. See [37, 38] for a general approach to construct anisotropic polyconvex energies.

The stored plastic energy ψ_{h} is, for simplicity, adopted in the form that accounts for the linear isotropic hardening,

$$\psi_{\mathrm{h}}(\bar{\gamma}) = \frac{1}{2} H \bar{\gamma}^2, \tag{12}$$

where $H \geq 0$ is the hardening parameter.

In the phase-field framework, the energy of the diffuse twin boundaries ψ_Γ is defined as a function of the order parameter η and its gradient $\nabla\eta$. Here, the so-called double-obstacle potential is adopted [39],

$$\begin{aligned} &\psi_\Gamma(\eta, \nabla\eta) = \Delta f\, \eta(1-\eta) + \kappa \nabla\eta \cdot \nabla\eta, \\ &\Delta f = \frac{4\Gamma}{\pi\ell}, \quad \kappa = \frac{4\Gamma\ell}{\pi}, \end{aligned} \tag{13}$$

where Δf is the height of the energy barrier for the formation of the twin interface and κ characterizes the gradient energy of the twin interface. Both parameters can be expressed in terms of Γ, the interfacial energy density (per unit area), and ℓ, the interface thickness parameter. Note that the theoretical thickness of an equilibrium (stress-free) interface is equal to $\pi\ell$ [39, 40].

Since the double-obstacle potential (13) is employed in the model, it is crucial to enforce the bound constraint $0 \leq \eta \leq 1$ (note the first term in ψ_Γ that tends to $-\infty$ for $\eta \to \pm\infty$). For this purpose, the indicator function $I_{[0,1]}$ is included in the free energy function (9), which is defined as

$$I_{[0,1]}(\eta) = \begin{cases} 0 & \text{if } 0 \leq \eta \leq 1, \\ +\infty & \text{otherwise.} \end{cases} \tag{14}$$

To avoid the complexity stemming from the non-differentiability of $I_{[0,1]}$, in the derivations in the reminder of Sect. 2, the indicator function $I_{[0,1]}$ is approximated by its regularized counterpart $I^{\varepsilon}_{[0,1]}$ which is convex and continuously differentiable and converges to $I_{[0,1]}$ for $\varepsilon \to \infty$. Note, however, that in the actual implementation the bound constraint $0 \leq \eta \leq 1$ is enforced exactly using the augmented Lagrangian method, as detailed in Sect. 3.

The free energy specified by Eq. (9) depends, through the interfacial energy term ψ_Γ, on the gradient of the order parameter, $\nabla\eta$. Accordingly, the order parameter is a non-local variable, which makes the direct computer implementation of the model difficult. To facilitate the implementation, the micromorphic approach is adopted [41, 42] in which a new variable χ, the micromorphic counterpart of η, is introduced into the model. The micromorphic variable χ is enforced to be close to η through a penalty term ψ_{pen} that is added to the free energy, and the gradient of χ is used to approximate the gradient of η in the interfacial energy contribution, thus $\psi_\Gamma(\eta, \nabla\eta) \approx \psi_\Gamma(\eta, \nabla\chi)$. Upon the micromorphic regularization, the free energy takes the following form,

$$\begin{aligned} &\psi_\mu(\mathbf{F}, \mathbf{F}_{\mathrm{in}}, \bar{\gamma}, \eta, \chi, \nabla\chi) \\ &\quad = \psi_{\mathrm{e}}(\mathbf{F}_{\mathrm{e}}, \eta) + \psi_{\mathrm{h}}(\bar{\gamma}) + \psi_\Gamma(\eta, \nabla\chi) \\ &\qquad + \psi_{\mathrm{pen}}(\eta, \chi) + I^{\varepsilon}_{[0,1]}(\eta), \end{aligned} \tag{15}$$

where

$$\psi_{\mathrm{pen}}(\eta, \chi) = \frac{1}{2}\epsilon_\mu (\eta - \chi)^2, \tag{16}$$

and ϵ_μ is the micromorphic penalty parameter. As a result, the order parameter η becomes a local variable, and the corresponding evolution equation can be solved locally at each material point (i.e., at each Gauss point in the finite-element implementation), as discussed below. Clearly, the micromorphic variable χ is a global variable so the above treatment does not affect the size of the problem.

For future use, the rate of change of the free energy is expressed in the following form, see [26] for details,

$$\begin{aligned} &\dot{\psi}_\mu(\dot{\mathbf{F}}, \dot{\bar{\gamma}}, \dot{\eta}, \dot{\chi}, \nabla\dot{\chi}) \\ &\quad = \mathbf{P} \cdot \dot{\mathbf{F}} - (1-\eta) \sum_{s=1}^{n_s} \left(\tau^s_{\mathrm{m}} \dot{\gamma}^s_{\mathrm{m}} + q |\dot{\gamma}^s_{\mathrm{m}}| \right) \\ &\qquad - \eta \sum_{s=1}^{n_s} \left(\tau^s_{\mathrm{p}} \dot{\gamma}^s_{\mathrm{p}} + q |\dot{\gamma}^s_{\mathrm{p}}| \right) - (\bar{\tau}_{\mathrm{tw}} + f_\eta)\dot{\eta} \\ &\qquad - f_\chi \dot{\chi} - \mathbf{f}_{\nabla\chi} \cdot \nabla\dot{\chi}, \end{aligned} \tag{17}$$

as a function of the rate quantities which include the slip rates that are gathered in the vector $\dot{\boldsymbol{\gamma}} = \{\dot{\boldsymbol{\gamma}}_{\mathrm{m}}, \dot{\boldsymbol{\gamma}}_{\mathrm{p}}\}$ with $\dot{\boldsymbol{\gamma}}_{\mathrm{m}} = \{\dot{\gamma}^1_{\mathrm{m}}, \ldots, \dot{\gamma}^{n_s}_{\mathrm{m}}\}$ and $\dot{\boldsymbol{\gamma}}_{\mathrm{p}} = \{\dot{\gamma}^1_{\mathrm{p}}, \ldots, \dot{\gamma}^{n_s}_{\mathrm{p}}\}$. Note that the dependence on the current state is not indicated to make the notation more compact. In Eq. (17), $\mathbf{P} = J\boldsymbol{\sigma}\mathbf{F}^{-\mathrm{T}}$ is the first Piola–Kirchhoff stress tensor, $\boldsymbol{\sigma}$ is the Cauchy stress tensor, and $J = \det\mathbf{F}$. Further, the thermodynamic driving forces conjugate to $\bar{\gamma}$, η, χ, and $\nabla\chi$ are defined as

$$\begin{aligned} &q = -\frac{\partial\psi_\mu}{\partial\bar{\gamma}}, \quad f_\eta = -\frac{\partial\psi_\mu}{\partial\eta}, \quad f_\chi = -\frac{\partial\psi_\mu}{\partial\chi}, \\ &\mathbf{f}_{\nabla\chi} = -\frac{\partial\psi_\mu}{\partial\nabla\chi}. \end{aligned} \tag{18}$$

The resolved shear stresses τ^s_{m} and τ^s_{p} are defined as the projections of the Mandel stress $\mathbf{M} = J\mathbf{F}^{\mathrm{T}}_{\mathrm{e}}\boldsymbol{\sigma}\mathbf{F}^{-\mathrm{T}}_{\mathrm{e}}$ on the

respective slip systems, and the Schmid-type resolved stress for twinning $\bar{\tau}_{\mathrm{tw}}$ is defined accordingly in terms of $\log \mathbf{U}_{\mathrm{tw}}$,

$$\begin{aligned}
\tau_{\mathrm{m}}^{s} &= \mathbf{M} \cdot (\mathbf{s}_{\mathrm{m}}^{s} \otimes \mathbf{n}_{\mathrm{m}}^{s}),\\
\tau_{\mathrm{p}}^{s} &= \mathbf{M} \cdot (\mathbf{s}_{\mathrm{p}}^{s} \otimes \mathbf{n}_{\mathrm{p}}^{s}),\\
\bar{\tau}_{\mathrm{tw}} &= \mathbf{M} \cdot \log \mathbf{U}_{\mathrm{tw}}.
\end{aligned} \tag{19}$$

To complete the specification of the constitutive functions, the dissipation potential D ought to be defined. The dissipation potential comprises contributions from twinning and from plastic slip in the matrix and in the twin,

$$D(\dot{\boldsymbol{\gamma}}, \dot{\eta}) = D_{\mathrm{m}}(\dot{\boldsymbol{\gamma}}_{\mathrm{m}}) + D_{\mathrm{p}}(\dot{\boldsymbol{\gamma}}_{\mathrm{p}}) + D_{\mathrm{tw}}(\dot{\eta}), \tag{20}$$

and each contribution is assumed to include rate-independent and viscous parts. Specifically, the plastic slip contributions, D_{m} and D_{p}, are adopted in the following form,

$$\begin{aligned}
D_{\mathrm{m}}(\dot{\boldsymbol{\gamma}}_{\mathrm{m}}) &= (1-\eta) \sum_{s=1}^{n_s} \tau_{\mathrm{m}}^{\mathrm{c},s} \left(|\dot{\gamma}_{\mathrm{m}}^{s}| + \frac{(\dot{\gamma}_{\mathrm{m}}^{s})^2}{2\dot{\gamma}_0} \right),\\
D_{\mathrm{p}}(\dot{\boldsymbol{\gamma}}_{\mathrm{p}}) &= \eta \sum_{s=1}^{n_s} \tau_{\mathrm{p}}^{\mathrm{c},s} \left(|\dot{\gamma}_{\mathrm{p}}^{s}| + \frac{(\dot{\gamma}_{\mathrm{p}}^{s})^2}{2\dot{\gamma}_0} \right),
\end{aligned} \tag{21}$$

where $\tau_{\mathrm{m}}^{\mathrm{c},s}$ and $\tau_{\mathrm{p}}^{\mathrm{c},s}$ are the critical resolved shear stresses that characterize the rate-independent thresholds for the plastic slip on each slip system in the matrix and in the twin, respectively, and $\dot{\gamma}_0$ is the reference slip rate. Analogously, the twinning contribution to the dissipation potential is adopted in the following form,

$$D_{\mathrm{tw}}(\dot{\eta}) = \tau_{\mathrm{tw}}^{\mathrm{c}} \gamma_{\mathrm{tw}} \left(|\dot{\eta}| + \frac{\dot{\eta}^2}{2\dot{\eta}_0} \right), \quad \dot{\eta}_0 = \frac{\pi v_0}{8\ell}, \tag{22}$$

where $\tau_{\mathrm{tw}}^{\mathrm{c}}$ is the critical resolved shear stress for twinning, and $\dot{\eta}_0$ is the reference rate that can be expressed in terms of v_0, the reference interface propagation speed, and ℓ, the interface thickness parameter.

The rate-dependent contribution to the dissipation potential D is treated here mostly as a regularization of the main, rate-independent part. In the applications, the loading rate is thus adjusted such that the viscous effects are not much pronounced. This is illustrated in Sect. 4.4. In order to capture physically-sound rate effects, the viscous part of the dissipation potential (the terms quadratic in $\dot{\boldsymbol{\gamma}}$ and $\dot{\eta}$) should be replaced by an adequate power law.

2.5 Variational formulation of the model

The variational formulation of the model follows the usual procedure in which the governing equations of the rate-problem are obtained by minimization of the global rate potential encompassing the rate of free energy and the dissipation potential [9, 40, 43–45].

The functional of the total potential energy $\mathcal{E}$ is defined as a sum of the total free energy functional $\Psi = \int_B \psi_\mu \mathrm{d}V$ and the potential of external loads Ω (assumed conservative) so that $\mathcal{E} = \Psi + \Omega$. Here, B denotes the domain occupied by the body in the reference configuration. The rate of the potential energy has thus the following form,

$$\begin{aligned}
\dot{\mathcal{E}}[\dot{\boldsymbol{\varphi}}, \dot{\boldsymbol{\gamma}}, \dot{\eta}, \dot{\boldsymbol{\chi}}] &= \dot{\Psi}[\dot{\boldsymbol{\varphi}}, \dot{\boldsymbol{\gamma}}, \dot{\eta}, \dot{\boldsymbol{\chi}}] + \dot{\Omega}[\dot{\boldsymbol{\varphi}}],\\
\dot{\Psi}[\dot{\boldsymbol{\varphi}}, \dot{\boldsymbol{\gamma}}, \dot{\eta}, \dot{\boldsymbol{\chi}}] &= \int_B \dot{\psi}_\mu(\nabla\dot{\boldsymbol{\varphi}}, \dot{\boldsymbol{\gamma}}, \dot{\eta}, \dot{\boldsymbol{\chi}}, \nabla\dot{\boldsymbol{\chi}}) \mathrm{d}V,
\end{aligned} \tag{23}$$

and the global rate-potential Π is defined as a sum of the potential energy rate $\dot{\mathcal{E}}$ and total dissipation potential $\mathcal{D}$,

$$\begin{aligned}
\Pi[\dot{\boldsymbol{\varphi}}, \dot{\boldsymbol{\gamma}}, \dot{\eta}, \dot{\boldsymbol{\chi}}] &= \dot{\mathcal{E}}[\dot{\boldsymbol{\varphi}}, \dot{\boldsymbol{\gamma}}, \dot{\eta}, \dot{\boldsymbol{\chi}}] + \mathcal{D}[\dot{\boldsymbol{\gamma}}, \dot{\eta}],\\
\mathcal{D}[\dot{\boldsymbol{\gamma}}, \dot{\eta}] &= \int_B D(\dot{\boldsymbol{\gamma}}, \dot{\eta}) \mathrm{d}V.
\end{aligned} \tag{24}$$

The complete evolution problem can now be formulated as a global minimization problem. Specifically, at each time instant, the current state is known, and the problem is to find the rate-solution $\{\dot{\boldsymbol{\varphi}}^*, \dot{\boldsymbol{\gamma}}^*, \dot{\eta}^*, \dot{\boldsymbol{\chi}}^*\}$ that minimizes the global rate-potential Π, namely

$$\{\dot{\boldsymbol{\varphi}}^*, \dot{\boldsymbol{\gamma}}^*, \dot{\eta}^*, \dot{\boldsymbol{\chi}}^*\} = \arg \min_{\dot{\boldsymbol{\varphi}}, \dot{\boldsymbol{\gamma}}, \dot{\eta}, \dot{\boldsymbol{\chi}}} \Pi[\dot{\boldsymbol{\varphi}}, \dot{\boldsymbol{\gamma}}, \dot{\eta}, \dot{\boldsymbol{\chi}}]. \tag{25}$$

Thanks to the micromorphic regularization, the free energy ψ_μ does not depend on the spatial gradient of η, see Eq. (15), and thus η can be considered a local variable so that the minimization with respect to $\dot{\eta}$ can be performed locally, at each material point. This is a great advantage of the micromorphic formulation considering the complexity of the minimization with respect to $\dot{\eta}$ (note the non-smoothness of the dissipation potential, the need for an adequate treatment of the bound constraint $0 \leq \eta \leq 1$, and the strong coupling in the evolution of η and plastic slips). In the finite-element implementation, this complexity can be handled much more efficiently locally, at each Gauss point, than on the global level.

The slip rates $\dot{\boldsymbol{\gamma}}$ are also local variables and minimization with respect to $\dot{\boldsymbol{\gamma}}$ can also be performed locally. The following local minimization problem can thus be formulated,

$$\{\dot{\boldsymbol{\gamma}}^*, \dot{\eta}^*\} = \arg \min_{\dot{\boldsymbol{\gamma}}, \dot{\eta}} \pi(\dot{\mathbf{F}}, \dot{\boldsymbol{\gamma}}, \dot{\eta}, \dot{\boldsymbol{\chi}}, \nabla\dot{\boldsymbol{\chi}}), \tag{26}$$

where π is the local rate-potential defined such that the global rate-potential is obtained as $\Pi = \int_B \pi \mathrm{d}V + \dot{\Omega}$, i.e.,

$$\pi(\dot{\mathbf{F}}, \dot{\boldsymbol{\gamma}}, \dot{\eta}, \dot{\boldsymbol{\chi}}, \nabla\dot{\boldsymbol{\chi}}) = \dot{\psi}_\mu(\dot{\mathbf{F}}, \dot{\boldsymbol{\gamma}}, \dot{\eta}, \dot{\boldsymbol{\chi}}, \nabla\dot{\boldsymbol{\chi}}) + D(\dot{\boldsymbol{\gamma}}, \dot{\eta}). \tag{27}$$

Upon solving the local minimization problem (26), the reduced local potential π^{red} can be defined,

$$\pi^{\mathrm{red}}(\dot{\mathbf{F}}, \dot{\chi}, \nabla\dot{\chi}) = \pi(\dot{\mathbf{F}}, \dot{\boldsymbol{\gamma}}^*, \dot{\eta}^*, \dot{\chi}, \nabla\dot{\chi}), \tag{28}$$

and the global variables $\dot{\boldsymbol{\varphi}}$ and $\dot{\chi}$ can then be found by minimizing the reduced global potential Π^{red},

$$\{\dot{\boldsymbol{\varphi}}^*, \dot{\chi}^*\} = \arg\min_{\dot{\boldsymbol{\varphi}}, \dot{\chi}} \Pi^{\mathrm{red}}[\dot{\boldsymbol{\varphi}}, \dot{\chi}],$$
$$\Pi^{\mathrm{red}}[\dot{\boldsymbol{\varphi}}, \dot{\chi}] = \int_B \pi^{\mathrm{red}}(\nabla\dot{\boldsymbol{\varphi}}, \dot{\chi}, \nabla\dot{\chi})\mathrm{d}V + \dot{\Omega}[\dot{\boldsymbol{\varphi}}]. \tag{29}$$

To reveal the structure of the actual problem to be solved, let us briefly discuss the governing equations resulting from the above variational formulation. The local rate-potential π is a convex, but non-smooth function of $\dot{\boldsymbol{\gamma}}$ and $\dot{\eta}$. The non-smoothness results from the rate-independent contributions to the dissipation potential, see Eqs. (21) and (22), and from the evolution law for the accumulated plastic slip $\bar{\gamma}$, see Eqs. (10) and (17). Accordingly, the following inclusions express the necessary and sufficient conditions for the minimum of π with respect to $\dot{\boldsymbol{\gamma}}$ and $\dot{\eta}$,

$$\mathbf{0} \in \partial_{\dot{\boldsymbol{\gamma}}}\pi(\dot{\mathbf{F}}, \dot{\boldsymbol{\gamma}}, \dot{\eta}, \dot{\chi}, \nabla\dot{\chi}), \quad 0 \in \partial_{\dot{\eta}}\pi(\dot{\mathbf{F}}, \dot{\boldsymbol{\gamma}}, \dot{\eta}, \dot{\chi}, \nabla\dot{\chi}), \tag{30}$$

where $\partial_{\dot{\boldsymbol{\gamma}}}\pi$ and $\partial_{\dot{\eta}}\pi$ are the subdifferentials of π [46]. These inclusions yield the following evolution equations for the individual slip rates $\dot{\gamma}_k^s$ (where $k \in \{\mathrm{m}, \mathrm{p}\}$, with 'm' and 'p' denoting the matrix and the twin, respectively) and for $\dot{\eta}$,

$$\dot{\gamma}_k^s = \dot{\gamma}_0 \,\mathrm{sign}(\tau_k^s)\, \frac{\langle |\tau_k^s| - (\tau_k^{\mathrm{c},s} + H\bar{\gamma})\rangle}{\tau_k^{\mathrm{c},s}},$$
$$\dot{\eta} = \dot{\eta}_0 \,\mathrm{sign}(\bar{\tau}_{\mathrm{tw}} + f_\eta)\, \frac{\langle |\bar{\tau}_{\mathrm{tw}} + f_\eta| - \tau_{\mathrm{tw}}^{\mathrm{c}}\gamma_{\mathrm{tw}}\rangle}{\tau_{\mathrm{tw}}^{\mathrm{c}}\gamma_{\mathrm{tw}}}, \tag{31}$$

where $\langle x\rangle = \frac{1}{2}(x + |x|)$ represents the Macauley bracket. It follows that a Perzyna-type flow rule is obtained with a rate-independent threshold and plastic slip rate (or twinning rate) proportional to the overstress.

On the global level, the reduced global potential Π^{red} is minimized with respect to the fields of $\dot{\boldsymbol{\varphi}}$ and $\dot{\chi}$. The condition of stationarity of the global potential Π^{red} with respect to $\dot{\boldsymbol{\varphi}}$ has the following form,

$$0 = \delta_{\dot{\boldsymbol{\varphi}}}\Pi^{\mathrm{red}}[\dot{\boldsymbol{\varphi}}, \dot{\chi}]$$
$$= \int_B \mathbf{P}\cdot\nabla\delta\boldsymbol{\varphi}\,\mathrm{d}V - \int_{\partial B_t} \bar{\mathbf{t}}\cdot\delta\boldsymbol{\varphi}\,\mathrm{d}S \quad \forall\,\delta\boldsymbol{\varphi}, \tag{32}$$

which is recognized as the virtual work principle, i.e., a weak form of the mechanical equilibrium equation with $\delta\boldsymbol{\varphi}$ as the test function that vanishes on the Dirichlet boundary. Here, to fix attention, the potential of the external loads has been assumed as $\Omega = \int_{\partial B_t} \bar{\mathbf{t}}\cdot\boldsymbol{\varphi}\,\mathrm{d}S$, which corresponds to the traction $\bar{\mathbf{t}}$ prescribed on the boundary ∂B_t.

The condition of stationarity of Π^{red} with respect to $\dot{\chi}$ has the following form,

$$0 = \delta_{\dot{\chi}}\Pi^{\mathrm{red}}[\dot{\boldsymbol{\varphi}}, \dot{\chi}]$$
$$= \int_B \left(\epsilon_\mu(\chi - \eta)\delta\chi + 2\kappa\nabla\chi\cdot\nabla\delta\chi\right)\mathrm{d}V \quad \forall\,\delta\chi, \tag{33}$$

which is a weak form of the Helmholtz-type PDE,[1]

$$\chi - \ell_\mu^2\nabla^2\chi = \eta, \quad \ell_\mu = \sqrt{\frac{2\kappa}{\epsilon_\mu}}, \tag{34}$$

with ℓ_μ as the corresponding characteristic length scale [41]. Since the global rate-potential Π does not involve any boundary terms involving the micromorphic variable χ, there is no boundary term in the weak form (33). This corresponds to the standard homogeneous Neumann boundary condition, $\nabla\chi\cdot\boldsymbol{\nu} = 0$, on the entire boundary ∂B with the outward normal $\boldsymbol{\nu}$. Other types of boundary conditions, in particular, the periodic boundary conditions used in the numerical examples, can be easily included in the framework (the details are omitted for brevity).

3 Incremental formulation and finite-element treatment

In Sect. 3.1, the phase-field model described in Sect. 2 is transformed to the incremental form to make it amenable to finite-element implementation. Subsequently, in Sect. 3.2, we present the augmented Lagrangian treatment of the non-smooth minimization problem. In Sect. 3.3, we discuss the different ways to solve the quasi-minimization problem. Finally, we elaborate on the finite-element discretization of the model in Sect. 3.4 and outline its computer implementation in Sect. 3.5.

3.1 Incremental (finite-step) formulation of the local minimization problem

In order to effectively solve the evolution problem, the rate equations discussed in Sect. 2.5 must be transformed to an incremental (finite-step) form. Consider thus a typical time increment $t_n \to t_{n+1} = t_n + \Delta t$ such that the solution at the previous time $t = t_n$ is known and the goal is to find the solution at the current time $t = t_{n+1}$. The superscripts n and $n+1$ will be used to denote the quantities at the previous and

[1] We acknowledge an oversight in our previous work [26], where the factor of 2 preceding κ and the power of 2 of the internal length scale ℓ were erroneously omitted from Eqs. (57) and (58).

current time steps, respectively. By applying the backward-Euler scheme, the rate variables are approximated in terms of the respective increments, for instance, $\dot{\eta} \approx \Delta\eta/\Delta t = (\eta^{n+1} - \eta^n)/\Delta t$.

Integration of the inelastic deformation gradient $\mathbf{F}_{\text{in}}$, accumulated plastic slip $\bar{\gamma}$ and dissipation potential D requires some attention. The evolution law for $\mathbf{F}_{\text{in}}$, cf. Eq. (8), is integrated using the volume-preserving exponential mapping [e.g. 47],

$$\mathbf{F}_{\text{in}}^{n+1} = \exp(\Delta t\, \mathbf{L}_{\text{in}}^{n+1})\mathbf{F}_{\text{in}}^{n}, \tag{35}$$

where

$$\Delta t\, \mathbf{L}_{\text{in}}^{n+1} = \left(1 - \tilde{\eta}^{n+1}\right) \sum_{s=1}^{n_{\text{s}}} \Delta\gamma_{\text{m}}^{s} \mathbf{s}_{\text{m}}^{s} \otimes \mathbf{n}_{\text{m}}^{s} + \tilde{\eta}^{n+1} \sum_{s=1}^{n_{\text{s}}} \Delta\gamma_{\text{p}}^{s} \mathbf{s}_{\text{p}}^{s} \otimes \mathbf{n}_{\text{p}}^{s} + \Delta\eta \log(\mathbf{U}_{\text{tw}}). \tag{36}$$

Consistent with the implicit backward-Euler scheme, the value of η is taken at t_{n+1} and the corresponding value is denoted by $\tilde{\eta}^{n+1}$. The reason to distinguish $\tilde{\eta}^{n+1}$ from the actual value $\eta^{n+1} = \eta^n + \Delta\eta$ is discussed below. Similarly, the accumulated plastic slip is integrated as, cf. Eq. (10),

$$\bar{\gamma}^{n+1} = \bar{\gamma}^{n} + (1 - \tilde{\eta}^{n+1}) \sum_{s=1}^{n_s} |\Delta\gamma_{\text{m}}^{s}| + \tilde{\eta}^{n+1} \sum_{s=1}^{n_s} |\Delta\gamma_{\text{p}}^{s}|. \tag{37}$$

Finally, the time-discrete dissipation potential $\Delta D \approx \Delta t\, D$ is defined as

$$\Delta D(\Delta\boldsymbol{\gamma}, \Delta\eta; \tilde{\eta}^{n+1}) = \Delta D_{\text{m}}\left(\Delta\boldsymbol{\gamma}_{\text{m}}; \tilde{\eta}^{n+1}\right) + \Delta D_{\text{p}}\left(\Delta\boldsymbol{\gamma}_{\text{p}}; \tilde{\eta}^{n+1}\right) + \Delta D_{\text{tw}}(\Delta\eta), \tag{38}$$

where

$$\Delta D_{\text{m}}(\Delta\boldsymbol{\gamma}_{\text{m}}; \tilde{\eta}^{n+1}) = (1 - \tilde{\eta}^{n+1}) \sum_{s=1}^{n_s} \tau_{\text{m}}^{\text{c},s} \left(|\Delta\gamma_{\text{m}}^{s}| + \frac{(\Delta\gamma_{\text{m}}^{s})^2}{2\Delta t\dot{\gamma}_0} \right), \tag{39}$$

$$\Delta D_{\text{p}}(\Delta\boldsymbol{\gamma}_{\text{p}}; \tilde{\eta}^{n+1}) = \tilde{\eta}^{n+1} \sum_{s=1}^{n_s} \tau_{\text{p}}^{\text{c},s} \left(|\Delta\gamma_{\text{p}}^{s}| + \frac{(\Delta\gamma_{\text{p}}^{s})^2}{2\Delta t\dot{\gamma}_0} \right), \tag{40}$$

$$\Delta D_{\text{tw}}(\Delta\eta) = \tau_{\text{tw}}^{\text{c}} \gamma_{\text{tw}} \left(|\Delta\eta| + \frac{\Delta\eta^2}{2\Delta t\dot{\eta}_0} \right). \tag{41}$$

Here and below, the variable $\tilde{\eta}^{n+1}$ is placed after a semicolon as an argument of a function to indicate its special status.

Our goal now is to reformulate the problem of minimization of the local rate-potential π, Eq. (26), in the finite-step setting. The minimization of π is performed with respect to the rates $\dot{\boldsymbol{\gamma}}$ and $\dot{\eta}$, which can be formally rewritten as the minimization with respect to the increments $\Delta\boldsymbol{\gamma}$ and $\Delta\eta$ through the substitution $\dot{\boldsymbol{\gamma}} = \Delta\boldsymbol{\gamma}/\Delta t$ and $\dot{\eta} = \Delta\eta/\Delta t$. This, however, must be done with care to preserve the consistency of the incremental finite-step problem with the reference rate-problem. Let us thus introduce the following time-discrete approximation of the rate-potential π,

$$\pi(\nabla\dot{\boldsymbol{\varphi}}, \dot{\boldsymbol{\gamma}}, \dot{\eta}, \dot{\boldsymbol{\chi}}, \nabla\dot{\boldsymbol{\chi}})\Big|_{t=t_{n+1}} \approx \frac{1}{\Delta t} \Delta\pi\left(\mathbf{f}, \Delta\boldsymbol{\gamma}, \Delta\eta; \tilde{\eta}^{n+1}\right), \tag{42}$$

where

$$\Delta\pi(\mathbf{f}, \Delta\boldsymbol{\gamma}, \Delta\eta; \tilde{\eta}^{n+1}) = \psi_{\mu}^{n+1}\left(\mathbf{f}, \Delta\boldsymbol{\gamma}, \Delta\eta; \tilde{\eta}^{n+1}\right) - \psi_{\mu}^{n} + \Delta D\left(\Delta\boldsymbol{\gamma}, \Delta\eta; \tilde{\eta}^{n+1}\right), \tag{43}$$

and vector $\mathbf{f}$ has been introduced which gathers the variables that are not the arguments in the local minimization problem,

$$\mathbf{f} = \{\mathbf{F}^{n+1}, \chi^{n+1}, \nabla\chi^{n+1}\}. \tag{44}$$

Note also that the dependence of $\Delta\pi$ on the known quantities from the previous time step $t = t_n$ is not indicated to make the notation more compact.

In Eq. (43), ψ_{μ}^{n} is the (known) free energy at t_n and ψ_{μ}^{n+1} is the free energy at t_{n+1} that is evaluated according to Eq. (15) with $\mathbf{F}_{\text{in}}^{n+1}$ specified by Eqs. (35) and (36) and with $\bar{\gamma}^{n+1}$ specified by Eq. (37),

$$\psi_{\mu}^{n+1}(\mathbf{f}, \Delta\boldsymbol{\gamma}, \Delta\eta; \tilde{\eta}^{n+1}) = \psi_{\mu}(\mathbf{F}^{n+1}, \mathbf{F}_{\text{in}}^{n+1}, \bar{\gamma}^{n+1}, \eta^{n+1}, \chi^{n+1}, \nabla\chi^{n+1}), \tag{45}$$

so that $\tilde{\eta}^{n+1}$ appears as an independent argument of ψ_{μ}^{n+1}. Even though $\tilde{\eta}^{n+1} = \eta^{n+1}$, the dependence on $\tilde{\eta}^{n+1}$ is indicated explicitly in order to distinguish this variable from $\eta^{n+1} = \eta^n + \Delta\eta$ that enters the equation for ψ_{μ}^{n+1} through ψ_{Γ}, ψ_{pen} and $I_{[0,1]}$, and also through the dependence of $\mathbb{L}$ on η in ψ_{e}. The reason for this treatment is that, in the time-discrete setting, the minimization with respect to $\dot{\eta}$ is transformed to the minimization with respect to $\Delta\eta$, and setting $\tilde{\eta}^{n+1} = \eta^n + \Delta\eta$ and performing a full minimization with respect to $\Delta\eta$ would cause an inconsistency with the rate problem. This can be most easily illustrated by considering the dissipative driving force as the derivative of ΔD

with respect to $\Delta\eta$, namely

$$\frac{\partial}{\partial\Delta\eta}\Delta D(\Delta\boldsymbol{\gamma},\Delta\eta;\tilde{\eta}^{n+1}) \neq \frac{\partial}{\partial\Delta\eta}\Delta\tilde{D}(\Delta\boldsymbol{\gamma},\Delta\eta), \tag{46}$$

where ΔD is given by Eqs. (38)–(41), while $\Delta\tilde{D}$ is defined as

$$\Delta\tilde{D}(\Delta\boldsymbol{\gamma},\Delta\eta) = \Delta D(\Delta\boldsymbol{\gamma},\Delta\eta;\eta^n+\Delta\eta). \tag{47}$$

Clearly, the left-hand side expression in Eq. (46) gives the correct dissipative driving force for twinning, i.e., that resulting solely from ΔD_{tw}, while the right-hand side expression includes additional incorrect terms resulting from the differentiation of ΔD_{m} and ΔD_{p} with respect to $\tilde{\eta}^{n+1}$. Similar incorrect contributions would occur if ψ_μ^{n+1} was differentiated with respect to $\tilde{\eta}^{n+1}$.

Accordingly, to preserve consistency with the problem (26) of minimization of the rate-potential π, the incremental (finite-step) evolution problem is formulated as the following minimization problem which is not a standard optimization problem, but rather a *quasi-optimization* problem,

$$\{\Delta\boldsymbol{\gamma}^*,\Delta\eta^*\} = \arg\min_{\Delta\boldsymbol{\gamma},\Delta\eta}\ \Delta\pi(\mathbf{f},\Delta\boldsymbol{\gamma},\Delta\eta;\eta^n+\Delta\eta^*). \tag{48}$$

Note that $\Delta\pi$ depends on both $\Delta\eta$, the variable with respect to which the minimization is performed, and $\Delta\eta^*$, the actual solution of the minimization problem. The peculiarity of the quasi-minimization problem is that the function that is minimized depends on the solution, as indicated in Eq. (48). This results here from the transition from the rate-problem to the incremental (finite-step) problem, see also [9]. Similar quasi-optimization problems, though not related to the finite-step setting, appear in frictional contact problems [48] and in non-potential problems in rate-independent plasticity [49].

3.2 Augmented Lagrangian treatment

The minimization problem (48) is non-smooth due to the rate-independent dissipation contributions to ΔD, see Eqs. (38)–(41), due to the absolute value function in the expression for $\bar{\gamma}^{n+1}$, see Eq. (37), and due to the indicator function $I_{[0,1]}(\eta)$ enforcing the bound constraint $0\le\eta\le 1$. An efficient computational scheme for this problem is developed by using the augmented Lagrangian method, which transforms the non-smooth minimization problem (48) to a smooth and unconstrained saddle-point problem, see [50] for details,

$$\begin{aligned}&\{\Delta\boldsymbol{\gamma}^*,\Delta\eta^*,\boldsymbol{\mu}^*,\lambda^*\}\\ &\quad=\min_{\Delta\boldsymbol{\gamma},\Delta\eta}\max_{\boldsymbol{\mu},\lambda} L(\mathbf{f},\Delta\boldsymbol{\gamma},\Delta\eta,\boldsymbol{\mu},\lambda;\eta^n+\Delta\eta^*),\end{aligned} \tag{49}$$

with the following Lagrange function L,

$$\begin{aligned}&L\left(\mathbf{f},\Delta\boldsymbol{\gamma},\Delta\eta,\boldsymbol{\mu},\lambda;\tilde{\eta}^{n+1}\right)\\ &\quad=\psi_\mu^{n+1}\left(\mathbf{f},\Delta\boldsymbol{\gamma},\Delta\eta;\tilde{\eta}^{n+1}\right)-\psi_\mu^n\\ &\qquad+\Delta D^{\mathrm{visc}}\left(\Delta\boldsymbol{\gamma},\Delta\eta;\tilde{\eta}^{n+1}\right)+\left(1-\tilde{\eta}^{n+1}\right)\\ &\qquad\times\sum_{s=1}^{n_s} l_\gamma\left(\Delta\gamma_{\mathrm{m}}^s,\mu_{\mathrm{m}}^s\right)+\tilde{\eta}^{n+1}\sum_{s=1}^{n_s} l_\gamma\left(\Delta\gamma_{\mathrm{p}}^s,\mu_{\mathrm{p}}^s\right)\\ &\qquad+l_\eta(\Delta\eta,\lambda),\end{aligned} \tag{50}$$

where ΔD^{visc} is the part of the dissipation potential ΔD that gathers the viscous (and smooth) dissipation contributions,

$$\begin{aligned}&\Delta D^{\mathrm{visc}}(\Delta\boldsymbol{\gamma},\Delta\eta;\tilde{\eta}^{n+1})\\ &\quad=(1-\tilde{\eta}^{n+1})\sum_{s=1}^{n_s}\tau_{\mathrm{m}}^{\mathrm{c},s}\frac{(\Delta\gamma_{\mathrm{m}}^s)^2}{2\Delta t\dot{\gamma}_0}+\tilde{\eta}^{n+1}\sum_{s=1}^{n_s}\tau_{\mathrm{p}}^{\mathrm{c},s}\frac{(\Delta\gamma_{\mathrm{p}}^s)^2}{2\Delta t\dot{\gamma}_0}\\ &\qquad+\tau_{\mathrm{tw}}^{\mathrm{c}}\gamma_{\mathrm{tw}}\frac{\Delta\eta^2}{2\Delta t\dot{\eta}_0},\end{aligned} \tag{51}$$

while the rate-independent contributions are handled by functions l_γ and l_η, to be specified below.

In addition to the primal variables $\Delta\boldsymbol{\gamma}$ and $\Delta\eta$, the Lagrange function L depends on the Lagrange multipliers $\boldsymbol{\mu}=\{\boldsymbol{\mu}_{\mathrm{m}},\boldsymbol{\mu}_{\mathrm{p}}\}$ and λ. Each vector of multipliers $\boldsymbol{\mu}_k=\{\mu_k^1,\ldots,\mu_k^{n_s}\}$ ($k\in\{\mathrm{m},\mathrm{p}\}$) is associated with the corresponding vector of slip increments $\Delta\boldsymbol{\gamma}_k=\{\Delta\gamma_k^1,\ldots,\Delta\gamma_k^{n_s}\}$. Likewise, the scalar multiplier λ is associated with the order parameter η.

As in the case of the quasi-minimization problem (48), the saddle-point problem is, in fact, a quasi-saddle-point problem in which the Lagrange function L depends on the solution $\Delta\eta^*$, and hence the dependence of L on $\tilde{\eta}^{n+1}$ is indicated in Eq. (50), similar to $\Delta\pi$ in Eq. (43). This is further discussed below.

Function l_η is responsible for handling the inequality constraints $0\le\eta\le 1$ and the rate-independent part of ΔD_{tw}, i.e., the term $\tau_{\mathrm{tw}}^{\mathrm{c}}\gamma_{\mathrm{tw}}|\Delta\eta|$ in Eq. (41). The following form of l_η is adopted after [50],

$$l_\eta(\Delta\eta,\lambda)=\begin{cases} l_\eta^{(1)} \text{ if } \hat{\lambda}\le\varrho_\eta\Delta\eta^- -\tau_{\mathrm{tw}}^{\mathrm{c}}\gamma_{\mathrm{tw}},\\ l_\eta^{(2)} \text{ if } \varrho_\eta\Delta\eta^- -\tau_{\mathrm{tw}}^{\mathrm{c}}\gamma_{\mathrm{tw}}<\hat{\lambda}<-\tau_{\mathrm{tw}}^{\mathrm{c}}\gamma_{\mathrm{tw}},\\ l_\eta^{(3)} \text{ if } -\tau_{\mathrm{tw}}^{\mathrm{c}}\gamma_{\mathrm{tw}}\le\hat{\lambda}\le\tau_{\mathrm{tw}}^{\mathrm{c}}\gamma_{\mathrm{tw}},\\ l_\eta^{(4)} \text{ if } \tau_{\mathrm{tw}}^{\mathrm{c}}\gamma_{\mathrm{tw}}<\hat{\lambda}<\varrho_\eta\Delta\eta^+ +\tau_{\mathrm{tw}}^{\mathrm{c}}\gamma_{\mathrm{tw}},\\ l_\eta^{(5)} \text{ if } \varrho_\eta\Delta\eta^+ +\tau_{\mathrm{tw}}^{\mathrm{c}}\gamma_{\mathrm{tw}}\le\hat{\lambda},\end{cases} \tag{52}$$

with

$$l_\eta^{(1)}=\lambda(\Delta\eta-\Delta\eta^-)+\frac{\varrho_\eta}{2}(\Delta\eta-\Delta\eta^-)^2-\tau_{\mathrm{tw}}^{\mathrm{c}}\gamma_{\mathrm{tw}}\Delta\eta^-,$$

$$l_\eta^{(2)}=-\frac{1}{2\varrho_\eta}\left(\lambda^2+2\tau_{\mathrm{tw}}^{\mathrm{c}}\gamma_{\mathrm{tw}}\hat{\lambda}+(\tau_{\mathrm{tw}}^{\mathrm{c}}\gamma_{\mathrm{tw}})^2\right),$$

$$l_\eta^{(3)} = \left(\lambda + \frac{\varrho_\eta}{2}\,\Delta\eta\right)\Delta\eta,$$
$$l_\eta^{(4)} = -\frac{1}{2\varrho_\eta}\left(\lambda^2 - 2\tau_{\rm tw}^{\rm c}\gamma_{\rm tw}\hat{\lambda} + (\tau_{\rm tw}^{\rm c}\gamma_{\rm tw})^2\right),$$
$$l_\eta^{(5)} = \lambda(\Delta\eta - \Delta\eta^+) + \frac{\varrho_\eta}{2}(\Delta\eta - \Delta\eta^+)^2 + \tau_{\rm tw}^{\rm c}\gamma_{\rm tw}\Delta\eta^+,$$

where $\hat{\lambda} = \lambda + \varrho_\eta\Delta\eta$ is the augmented Lagrange multiplier, $\varrho_\eta > 0$ is a regularization parameter, and $\Delta\eta^- = -\eta^n \le 0$ and $\Delta\eta^+ = 1 - \eta^n \ge 0$ are the bounds for the increment of the order parameter, $\Delta\eta^- \le \Delta\eta \le \Delta\eta^+$. Note that a single Lagrange multiplier is used to handle both the rate-independent dissipation and the bound constraint.

The rate-independent dissipation associated with plastic slip is handled by function l_γ which can be seen as a special case of function l_η specified above. Since no bound constraints are enforced on slip increments, l_γ involves only three branches that correspond to the second, third, and fourth branches of l_η. Function l_γ is thus defined as follows,

$$l_\gamma(\Delta\gamma_k^s, \mu_k^s) = \begin{cases} l_\gamma^{(1)} & \text{if } \hat{\mu}_k^s < -\tau_k^{{\rm c},s}, \\ l_\gamma^{(2)} & \text{if } -\tau_k^{{\rm c},s} \le \hat{\mu}_k^s \le \tau_k^{{\rm c},s}, \\ l_\gamma^{(3)} & \text{if } \tau_k^{{\rm c},s} < \hat{\mu}_k^s, \end{cases} \tag{53}$$

with

$$l_\gamma^{(1)} = -\frac{1}{2\varrho_\gamma}\left((\mu_k^s)^2 + 2\,\tau_k^{{\rm c},s}\,\hat{\mu}_k^s + (\tau_k^{{\rm c},s})^2\right),$$
$$l_\gamma^{(2)} = \left(\mu_k^s + \frac{\varrho_\gamma}{2}\,\Delta\gamma_k^s\right)\Delta\gamma_k^s,$$
$$l_\gamma^{(3)} = -\frac{1}{2\varrho_\gamma}\left((\mu_k^s)^2 - 2\,\tau_k^{{\rm c},s}\,\hat{\mu}_k^s + (\tau_k^{{\rm c},s})^2\right),$$

where $\hat{\mu}_k^s = \mu_k^s + \varrho_\gamma\Delta\gamma_k^s$ is the augmented Lagrange multiplier, and $\varrho_\gamma > 0$. For each pair $(\Delta\gamma_k^s, \mu_k^s)$, function $l_\gamma(\Delta\gamma_k^s, \mu_k^s)$ introduces the augmented Lagrangian treatment of the corresponding term $\tau_k^{{\rm c},s}|\Delta\gamma_k^s|$ in the dissipation potential ΔD_k, cf. Eqs. (39)–(40).

Note that the non-smoothness of the terms $|\Delta\gamma_k^s|$ in the expression for $\bar{\gamma}^{n+1}$ in Eq. (37) can be naturally treated using the corresponding Lagrange multiplier μ_k^s (or $\hat{\mu}_k^s$),

$$|\Delta\gamma_k^s| = {\rm sign}(\mu_k^s)\Delta\gamma_k^s. \tag{54}$$

Since the ill-conditioning of ${\rm sign}(\mu_k^s)$ at $\mu_k^s \approx 0$ occurs only when $\Delta\gamma_k^s = 0$, the product of the two terms behaves well.

The solution of the saddle-point problem (49) is found by solving the nonlinear equation $\mathbf{Q} = \mathbf{0}$ expressing the stationarity of L with respect to the primal variables $(\Delta\boldsymbol{\gamma}, \Delta\eta)$ and Lagrange multipliers $(\boldsymbol{\mu}, \lambda)$,

$$\mathbf{Q}(\mathbf{f}, \mathbf{h}) = \left.\frac{\partial L(\mathbf{f}, \Delta\boldsymbol{\gamma}, \Delta\eta, \boldsymbol{\mu}, \lambda; \tilde{\eta}^{n+1})}{\partial\{\Delta\boldsymbol{\gamma}, \Delta\eta, \boldsymbol{\mu}, \lambda\}}\right|_{\tilde{\eta}^{n+1}=\eta^n+\Delta\eta} = \mathbf{0}. \tag{55}$$

For future use, the unknowns are here assembled in vector $\mathbf{h}$,

$$\mathbf{h} = \{\Delta\boldsymbol{\gamma}, \Delta\eta, \boldsymbol{\mu}, \lambda\}. \tag{56}$$

Consistent with the quasi-optimization structure of the minimization problem (48) and of the resulting saddle-point problem (49), $\tilde{\eta}^{n+1}$ is treated as an independent variable when L is differentiated with respect to $\Delta\eta$, and only after the differentiation, $\tilde{\eta}^{n+1}$ is substituted by $\eta^n + \Delta\eta$, as indicated in Eq. (55).

The essence of the augmented Lagrangian technique is in enforcing state-dependent constraints on either the primal or dual variables. Consider, for instance, function l_η defined by Eq. (52) which involves five branches, each corresponding to a different state that is determined in terms of the augmented Lagrange multiplier $\hat{\lambda}$. The first and the last branch correspond to the active bound constraints. The second and the fourth branch correspond to, respectively, the backward and forward transformation. Finally, the third branch corresponds to a halted transformation. Depending on the state, the condition of stationarity of L with respect to the Lagrange multiplier λ enforces the condition $\Delta\eta = \Delta\eta^\pm$ (active bound constraint), $\Delta\eta = 0$ (halted transformation), or $\lambda = \pm\tau_{\rm tw}^{\rm c}\gamma_{\rm tw}$ (forward or backward transformation). For more details, the reader is referred to [50], and related applications of the augmented Lagrangian method can be found in [40, 42].

It can be checked that equation $\mathbf{Q} = \mathbf{0}$ is ill-posed when $\eta^{n+1} = 0$ or $\eta^{n+1} = 1$. Consider, for instance, the derivative of L with respect to $\Delta\gamma_{\rm p}^s$. Since all the terms in L that involve $\Delta\gamma_{\rm p}^s$, see Eqs. (36), (37), (50), and (51), are premultiplied by $\tilde{\eta}^{n+1}$, the resulting derivative of L is identically equal to zero when $\tilde{\eta}^{n+1} = 0$. A well-posed formulation can be obtained by scaling the corresponding equations by $1/\eta^{n+1}$. A similar argument applies to the derivative of L with respect to $\Delta\gamma_{\rm m}^s$ when $\eta^{n+1} = 1$, and a remedy is to scale the corresponding equations by $1/(1 - \eta^{n+1})$. Accordingly, the unknowns are grouped into three vectors $\mathbf{h}_{\rm m} = \{\Delta\gamma_{\rm m}^s, \mu_{\rm m}^s\}$, $\mathbf{h}_{\rm p} = \{\Delta\gamma_{\rm p}^s, \mu_{\rm p}^s\}$, and $\mathbf{h}_\eta = \{\Delta\eta, \lambda\}$, and the Lagrange function is formally rewritten as $L = L(\mathbf{f}, \mathbf{h}_{\rm m}, \mathbf{h}_{\rm p}, \mathbf{h}_\eta; \tilde{\eta}^{n+1})$. The following scaled local residual is then introduced,

$$\hat{\mathbf{Q}}(\mathbf{f}, \mathbf{h}) = \{\hat{\mathbf{Q}}_{\rm m}, \hat{\mathbf{Q}}_{\rm p}, \mathbf{Q}_\eta\} = \mathbf{0}, \tag{57}$$

where

$$\hat{\mathbf{Q}}_{\mathrm{m}} = \frac{1}{1-\eta^{n+1}}\mathbf{Q}_{\mathrm{m}} = \frac{1}{1-\eta^{n+1}}\frac{\partial L(\mathbf{f}, \mathbf{h}_{\mathrm{m}}, \mathbf{h}_{\mathrm{p}}, \mathbf{h}_{\eta}; \eta^{n+1})}{\partial \mathbf{h}_{\mathrm{m}}}, \tag{58}$$

$$\hat{\mathbf{Q}}_{\mathrm{p}} = \frac{1}{\eta^{n+1}}\mathbf{Q}_{\mathrm{p}} = \frac{1}{\eta^{n+1}}\frac{\partial L(\mathbf{f}, \mathbf{h}_{\mathrm{m}}, \mathbf{h}_{\mathrm{p}}, \mathbf{h}_{\eta}; \eta^{n+1})}{\partial \mathbf{h}_{\mathrm{p}}}, \tag{59}$$

$$\mathbf{Q}_{\eta} = \left.\frac{\partial L(\mathbf{f}, \mathbf{h}_{\mathrm{m}}, \mathbf{h}_{\mathrm{p}}, \mathbf{h}_{\eta}; \tilde{\eta}^{n+1})}{\partial \mathbf{h}_{\eta}}\right|_{\tilde{\eta}^{n+1}=\eta^{n}+\Delta\eta}, \tag{60}$$

and $\eta^{n+1} = \eta^n + \Delta\eta$. Note that the special treatment of $\tilde{\eta}^{n+1}$ resulting from the quasi-optimization structure of the minimization problem (48) is needed only when the differentiation with respect to $\Delta\eta$ is performed, and thus concerns only $\mathbf{Q}_{\eta}$ in Eq. (60). The scaling-based approach presented above follows that developed in [50] in the context of a macroscopic model of pseudoelasticity.

The modified stationarity condition (57) can now be solved using the Newton method. At each Newton iteration, a linear problem is solved and the solution is updated according to

$$\mathbf{h}^{i+1} = \mathbf{h}^{i} + \Delta\mathbf{h}^{i}, \quad \Delta\mathbf{h}^{i} = -\left(\frac{\partial \hat{\mathbf{Q}}}{\partial \mathbf{h}}\right)^{-1}\hat{\mathbf{Q}}(\mathbf{f}, \mathbf{h}^{i}). \tag{61}$$

Once a converged solution is obtained, the unknown vector $\mathbf{h}$ is an implicit function of $\mathbf{f}$, thus $\mathbf{h} = \mathbf{h}(\mathbf{f})$. The sensitivity of $\mathbf{h}$ with respect to $\mathbf{f}$ is then computed in a standard way [51, 52],

$$\frac{\partial \mathbf{h}}{\partial \mathbf{f}} = -\left(\frac{\partial \hat{\mathbf{Q}}}{\partial \mathbf{h}}\right)^{-1}\frac{\partial \hat{\mathbf{Q}}}{\partial \mathbf{f}}. \tag{62}$$

This sensitivity will be used to compute the global tangent matrix.

3.3 Approximation of the quasi-minimization problem

As discussed in Sect. 3.1, in order to preserve consistency with the rate evolution problem (26), the incremental (finite-step) problem (48) is formulated as a quasi-minimization problem. The quasi-optimization structure of the incremental problem does not lead to any major difficulties in its practical application and computer implementation. Nevertheless, below we briefly discuss two approximate approaches that lead to genuine minimization problems. In both cases, the augmented Lagrangian treatment of the non-smooth minimization follows exactly the route outlined in Sect. 3.2 and is not discussed in detail.

In the first approach, the variable $\tilde{\eta}^{n+1}$ as an argument of the incremental potential $\Delta\pi$ is replaced by the corresponding value from the previous time step, η^n, thus

$$\{\Delta\boldsymbol{\gamma}^{*}, \Delta\eta^{*}\} = \arg\min_{\Delta\boldsymbol{\gamma}, \Delta\eta} \Delta\pi(\mathbf{f}, \Delta\boldsymbol{\gamma}, \Delta\eta; \eta^{n}). \tag{63}$$

At the current time t_{n+1}, η^n is known and, for a sufficiently small time increment, can be considered as a good approximation of η^{n+1}. Accordingly, the solution of the minimization problem (63) will approximate the solution of the quasi-minimization problem (48).

In the second approach, a full minimization of $\Delta\pi$ with respect to $\Delta\eta$ is performed, considering also the dependence of $\Delta\pi$ on $\tilde{\eta}^{n+1}$ with $\tilde{\eta}^{n+1} = \eta^n + \Delta\eta$, thus

$$\{\Delta\boldsymbol{\gamma}^{*}, \Delta\eta^{*}\} = \arg\min_{\Delta\boldsymbol{\gamma}, \Delta\eta} \Delta\pi(\mathbf{f}, \Delta\boldsymbol{\gamma}, \Delta\eta; \eta^{n} + \Delta\eta). \tag{64}$$

This will generate additional terms in the driving force for transformation, see e.g. Eq. (46), and thus result in an inexact solution.

We have performed a series of computations with the aim to examine the effects introduced by the above approximations. The problem considered in Sect. 4 has been used for that purpose and also a simple problem of growth and propagation of a single twin nucleus (see Sect. 5.3 in [26]). The latter could be solved with significantly coarser mesh and larger time steps. The results of those additional studies indicate that the above approximations do not visibly affect the results (we do not report the corresponding results since the differences are insignificant and even hard to detect). However, this may not be a generally valid conclusion. Hence, the consistent formulation is preferred here, and it is thus employed in the numerical examples.

3.4 Finite-element approximation

The variational framework developed in Sect. 2.5 for the rate-evolution problem leads to the global minimization problem for the fields $\dot{\boldsymbol{\varphi}}$ and $\dot{\boldsymbol{\chi}}$, cf. Eq. (29). However, in the incremental setting, a quasi-minimization problem is obtained, as discussed in Sect. 3.1 in the context of the local minimization problem (48). The quasi-optimization structure is then transferred also to the global incremental problem. Although this path could be followed in the development of the finite-element formulation for the global problem, a more compact formulation is presented below that takes the weak forms (32) and (33) as the starting point. An alternative formulation that is even more compact and also more convenient for the finite-element implementation is discussed at the end of this section.

Consider thus the two governing equations: the virtual work principle, Eq. (32), and the weak form of the Helmholtz-type PDE for the micromorphic variable $\boldsymbol{\chi}$, Eq. (33); and

rewrite them in the following compact form,

$$\mathcal{G}_{\mathbf{u}}[\mathbf{u}, \delta\mathbf{u}; \chi, \mathbf{h}] = 0 \quad \forall\, \delta\mathbf{u}, \tag{65}$$

$$\mathcal{G}_{\chi}[\chi, \delta\chi; \mathbf{u}, \mathbf{h}] = 0 \quad \forall\, \delta\chi, \tag{66}$$

where the deformation mapping $\boldsymbol{\varphi}$ has been replaced by the displacement $\mathbf{u}$ (note that $\boldsymbol{\varphi} = \mathbf{X} + \mathbf{u}$ and $\delta\boldsymbol{\varphi} = \delta\mathbf{u}$) in accordance with the common practice in the displacement-based finite element method. Here and in the following, the superscript $(n+1)$ denoting the current time step is omitted for brevity, since all quantities refer to the current time step. Since the stress tensor $\mathbf{P}$ in Eq. (32) depends on $\Delta\boldsymbol{\gamma}$ and $\Delta\eta$ (both contained in $\mathbf{h}$), and the order parameter η (also contained in $\mathbf{h}$) directly enters the weak form (33), the dependence of $\mathcal{G}_{\mathbf{u}}$ and $\mathcal{G}_{\chi}$ on $\mathbf{h}$ is explicitly indicated in Eqs. (65) and (66).

The global fields of $\mathbf{u}$ and χ are approximated using the respective finite-element basis functions $N_i^{(\mathbf{u})}$ and $N_i^{(\chi)}$,

$$\mathbf{u}^h = \sum_i N_i^{(\mathbf{u})} \mathbf{u}_i = \mathbf{N}^{(\mathbf{u})} \cdot \mathbf{p}_{\mathbf{u}}, \tag{67}$$

$$\chi^h = \sum_i N_i^{(\chi)} \chi_i = \mathbf{N}^{(\chi)} \cdot \mathbf{p}_{\chi}, \tag{68}$$

where $\mathbf{u}_i$ and χ_i denote the respective nodal values, and $\mathbf{p}_{\mathbf{u}} = \{\mathbf{u}_1, \mathbf{u}_2, \ldots\}$ and $\mathbf{p}_{\chi} = \{\chi_1, \chi_2, \ldots\}$ are the respective global vectors. The discretized weak forms are then obtained by substituting in $\mathcal{G}_{\mathbf{u}}$ and $\mathcal{G}_{\chi}$ the fields of $\mathbf{u}$ and χ by their approximations $\mathbf{u}^h$ and χ^h,

$$\mathcal{G}_{\mathbf{u}}^h(\mathbf{p}_{\mathbf{u}}, \delta\mathbf{p}_{\mathbf{u}}; \mathbf{p}_{\chi}, \mathbf{H}) = \mathcal{G}_{\mathbf{u}}[\mathbf{u}^h, \delta\mathbf{u}^h; \chi^h, \mathbf{h}(\mathbf{f}^h)] = 0 \quad \forall\, \delta\mathbf{p}_{\mathbf{u}}, \tag{69}$$

$$\mathcal{G}_{\chi}^h(\mathbf{p}_{\chi}, \delta\mathbf{p}_{\chi}; \mathbf{p}_{\mathbf{u}}, \mathbf{H}) = \mathcal{G}_{\chi}[\chi^h, \delta\chi^h; \mathbf{u}^h, \mathbf{h}(\mathbf{f}^h)] = 0 \quad \forall\, \delta\mathbf{p}_{\chi}. \tag{70}$$

Here $\mathbf{f}^h$ denotes the approximation of $\mathbf{f}$ evaluated in terms of $\mathbf{u}^h$ and χ^h, $\mathbf{h}(\mathbf{f}^h)$ denotes the local unknowns evaluated in terms of $\mathbf{f}^h$, and $\mathbf{H} = \{\mathbf{h}_1, \mathbf{h}_2, \ldots\}$ denotes the vector composed of the local vectors $\mathbf{h}_g$ $(g = 1, 2, \ldots)$ at all integration (Gauss) points.

Since the discretized weak forms $\mathcal{G}_{\mathbf{u}}^h$ and $\mathcal{G}_{\chi}^h$ are linear in $\delta\mathbf{p}_{\mathbf{u}}$ and $\delta\mathbf{p}_{\chi}$, respectively, they can be equivalently written in terms of the respective global residual vectors $\mathbf{R}_{\mathbf{u}}$ and $\mathbf{R}_{\chi}$,

$$\mathcal{G}_{\mathbf{u}}^h(\mathbf{p}_{\mathbf{u}}, \delta\mathbf{p}_{\mathbf{u}}; \mathbf{p}_{\chi}, \mathbf{H}) = \mathbf{R}_{\mathbf{u}}(\mathbf{p}_{\mathbf{u}}; \mathbf{p}_{\chi}, \mathbf{H}) \cdot \delta\mathbf{p}_{\mathbf{u}} = 0 \quad \forall\, \delta\mathbf{p}_{\mathbf{u}}, \tag{71}$$

$$\mathcal{G}_{\chi}^h(\mathbf{p}_{\chi}, \delta\mathbf{p}_{\chi}; \mathbf{p}_{\mathbf{u}}, \mathbf{H}) = \mathbf{R}_{\chi}(\mathbf{p}_{\chi}; \mathbf{p}_{\mathbf{u}}, \mathbf{H}) \cdot \delta\mathbf{p}_{\chi} = 0 \quad \forall\, \delta\mathbf{p}_{\chi}. \tag{72}$$

Following the standard argument, this leads to the following set of coupled nonlinear algebraic equations,

$$\mathbf{R}_{\mathbf{u}}(\mathbf{p}_{\mathbf{u}}; \mathbf{p}_{\chi}, \mathbf{H}) = \mathbf{0}, \quad \mathbf{R}_{\chi}(\mathbf{p}_{\chi}; \mathbf{p}_{\mathbf{u}}, \mathbf{H}) = \mathbf{0}. \tag{73}$$

In the monolithic solution scheme adopted in this work, both equations are solved simultaneously with respect to all global unknowns, hence

$$\mathbf{R}(\mathbf{p}, \mathbf{H}) = \mathbf{0}, \quad \mathbf{R} = \{\mathbf{R}_{\mathbf{u}}, \mathbf{R}_{\chi}\}, \quad \mathbf{p} = \{\mathbf{p}_{\mathbf{u}}, \mathbf{p}_{\chi}\}. \tag{74}$$

The above residual form of the discretized global equations can be derived in an alternative way, which is actually followed in our computer implementation. Consider thus the following functional of potential energy, cf. Eq. (23),

$$\mathcal{E}[\boldsymbol{\varphi}, \chi, \mathbf{h}] = \int_B \psi_{\mu}^{n+1}(\mathbf{f}, \mathbf{h}) \mathrm{d}V + \Omega[\boldsymbol{\varphi}], \tag{75}$$

that corresponds to the incremental formulation at t_{n+1} with $\psi_{\mu}^{n+1}(\mathbf{f}, \mathbf{h}) = \psi_{\mu}^{n+1}(\mathbf{f}, \Delta\boldsymbol{\gamma}, \Delta\eta; \eta^n + \Delta\eta)$ and $\tilde{\eta}^{n+1} = \eta^n + \Delta\eta$, cf. Eq. (45). The discretized form of $\mathcal{E}$ is obtained by introducing the finite-element approximation (67), thus

$$\mathcal{E}^h(\mathbf{p}, \mathbf{H}) = \mathcal{E}[\boldsymbol{\varphi}^h, \chi^h, \mathbf{h}^h], \tag{76}$$

where, as above, $\mathbf{p} = \{\mathbf{p}_{\mathbf{u}}, \mathbf{p}_{\chi}\}$ and $\mathbf{H} = \{\mathbf{h}_1, \mathbf{h}_2, \ldots\}$.

It can be checked that stationarity of $\mathcal{E}$ with respect to $\boldsymbol{\varphi}$ yields the virtual work principle (32) and stationarity with respect to χ yields the weak form (33). In the discrete setting, this corresponds to stationarity of $\mathcal{E}^h$ with respect to $\mathbf{p}$ [52, 53], which thus defines the residual $\mathbf{R}$, cf. Eq. (74),

$$\mathbf{R}(\mathbf{p}, \mathbf{H}) = \frac{\partial \mathcal{E}^h(\mathbf{p}, \mathbf{H})}{\partial \mathbf{p}} = \mathbf{0}. \tag{77}$$

The unknown in the nonlinear equation $\mathbf{R} = \mathbf{0}$ is the global vector $\mathbf{p}$, while the local variables assembled in vector $\mathbf{H} = \{\mathbf{h}_1, \mathbf{h}_2, \ldots\}$ are governed by the local equations that are solved at each integration (Gauss) point, cf. Eq. (57),

$$\hat{\mathbf{Q}}_g(\mathbf{f}_g(\mathbf{p}_e), \mathbf{h}_g) = \mathbf{0}, \quad g = 1, 2, \ldots. \tag{78}$$

Here the subscript g refers to the Gauss point, and $\mathbf{p}_e$ denotes a subset of the global vector $\mathbf{p}$, specifically those unknowns on which the e-th element explicitly depends. Recall that vector $\mathbf{f}_g$ comprises the deformation gradient $\mathbf{F}$ as well as the micromorphic variable χ and its gradient $\nabla\chi$, cf. Eq. (44), and the dependence of $\mathbf{f}_g$ on $\mathbf{p}_e$ is through the finite-element approximation (67).

The complete problem has the structure of a (path-dependent) coupled system [51] (or locally-coupled system in the terminology of [52]). The solution is obtained using the Newton method in an iterative–subiterative scheme, just like

in the classical elastoplasticity [51]. The local problems (78) are solved in the inner loops at individual Gauss points, and the global problem (77) is solved in the outer loop.

In practice, the global residual $\mathbf{R}$ is computed at the element level,

$$\mathbf{R} = \sum_e \mathbf{R}_e, \quad \mathbf{R}_e = \sum_g w_g \mathbf{R}_g,$$
$$\mathbf{R}_g = J_g \frac{\partial \psi_\mu(\mathbf{f}_g, \mathbf{h}_g)}{\partial \mathbf{f}_g} \frac{\partial \mathbf{f}_g}{\partial \mathbf{p}_e}, \tag{79}$$

where the first summation corresponds to the assembly of the element contributions and the second summation corresponds to the numerical integration over the element volume with w_g denoting the Gauss-point weight and J_g denoting the Jacobian of the transformation from the reference coordinate system to the global one. This operation is performed at each global iteration, and the Gauss-point contribution $\mathbf{R}_g$ is computed after the corresponding local problem $\hat{\mathbf{Q}}_g = \mathbf{0}$ is solved, thus yielding $\mathbf{h}_g = \mathbf{h}_g(\mathbf{f}_g)$.

The global tangent matrix $\mathbf{K}$ is also computed at the element level. Considering that $\mathbf{R}_g = \mathbf{R}_g(\mathbf{p}_e, \mathbf{h}_g)$ and $\mathbf{h}_g = \mathbf{h}_g(\mathbf{f}_g(\mathbf{p}_e))$, linearization of $\mathbf{R}_g$ with respect to $\mathbf{p}_e$ gives the following formula for the tangent matrix,

$$\mathbf{K} = \sum_e \mathbf{K}_e, \quad \mathbf{K}_e = \sum_g w_g \mathbf{K}_g,$$
$$\mathbf{K}_g = \frac{\partial \mathbf{R}_g}{\partial \mathbf{p}_e} - \frac{\partial \mathbf{R}_g}{\partial \mathbf{h}_g} \left(\frac{\partial \hat{\mathbf{Q}}_g}{\partial \mathbf{h}_g} \right)^{-1} \frac{\partial \hat{\mathbf{Q}}_g}{\partial \mathbf{f}_g} \frac{\partial \mathbf{f}_g}{\partial \mathbf{p}_e}, \tag{80}$$

where the derivative of the implicit dependence of $\mathbf{h}_g$ on $\mathbf{f}_g$ has been accounted for according to Eq. (62). The tangent matrix has the classical structure of the consistent tangent operator in elastoplasticity [51, 52], here applied to a coupled problem involving the displacement $\mathbf{u}$ and the micromorphic variable χ as the global unknown fields.

One of the goals of the detailed analysis carried out in Sect. 4 is to examine the performance and computational efficiency of several finite-element approximations. The implementation and the analysis are limited to 2D problems and to quadrilateral elements. Since the problem at hand is a coupled problem, various combinations of the approximations of the displacement $\mathbf{u}$ and micromorphic variable χ can be adopted. Concerning the displacement, three basic element topologies are considered, namely four-node element with bilinear shape functions (Q1), eight-node element with serendipity shape functions (Q2s), and nine-node element with quadratic shape functions (Q2).

The same class of shape functions is utilized for the micromorphic variable. However, it is essential to note that we restrict the interpolation order of the micromorphic variable to not surpass that of the displacement. The rationale behind this choice stems from the fact that although a higher discretization order of the micromorphic variable increases the resolution of the order parameter and thus of the interfacial energy, such a heightened resolution deems unnecessary in view of the relatively lower resolution of the strains and stresses. At the same time, spurious stress oscillations may arise due to inconsistent approximations of the deformation gradients $\mathbf{F}$ and $\mathbf{F}_{\text{tw}}$, which are dictated, respectively, by the discretization order of the displacement and the micromorphic variable. It is noteworthy that the spurious oscillations may also appear when employing the same discretization order for the two fields, particularly, in the case of low-order bilinear interpolation [31], but, as confirmed in our simulation results, the corresponding effects do not make a visible overall contribution if the mesh is sufficiently fine. In the case of bilinear shape functions for the two fields, adopting a constant $\mathbf{F}_{\text{tw}}$ within the element would eliminate the issue [9], which is, however, not pursued here.

In analogy to the displacements, the interpolation order of the micromorphic variable is denoted by H1, H2s, and H2, so that, for instance, Q1H1 denotes the element with bilinear shape functions used for both the displacement and the micromorphic variable. Considering that the bilinear elements are known to be prone to locking, the F-bar formulation [54] is also considered, and the corresponding element is denoted by Q1H1-Fbar.

By default, the full Gaussian quadrature is used, namely 2×2 Gauss integration for Q1 elements and 3×3 Gauss integration for Q2s and Q2 elements (the quadrature order is specified with respect to the order of interpolation of the displacement field). In the case of the serendipity elements (Q2s), a reduced 2×2 Gauss integration is also considered. This is indicated by an 'R' at the end of the element name so that, for instance, Q2sH1-R denotes the Q2sH1 element with reduced integration. Altogether, eight different combinations of the shape functions and integration order are used in the computational study, and these are illustrated in Fig. 2.

3.5 Computer implementation

Implementation and finite-element computations have been performed using the *AceGen*/*AceFEM* system [52, 53]. The implementation is largely facilitated by the automatic differentiation (AD) technique used in *AceGen*, and the above formulation, Eqs. (75)–(80), is particularly suitable for the AD-based approach.

All computations have been carried out on the same workstation so that the wall-clock time can be used as a measure of the computational cost. The workstation is equipped with two CPUs (Intel Xenon CPU E5-2680 v3 @2.50GHz, each with 12 cores) and with 128 GB RAM. Assembly of element quantities (residual vector and tangent matrix) is fully parallelized, and all computer resources are used at this stage.

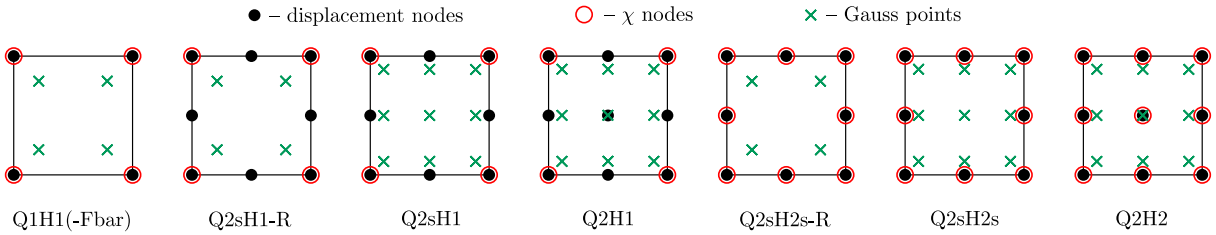

Fig. 2 Elements used in the computational study

On the other hand, a direct solver (Intel MKL PARDISO) is employed to solve the system of linear equations at each Newton iteration. As it is well known, direct linear solvers have inherent limitations in terms of scalability.

In the computational scheme, the evolution problem is solved using an adaptive time incrementation algorithm. In this algorithm, the next time increment is adjusted based on the current convergence behavior. Specifically, the time increment is increased or decreased if the current number of iterations needed to achieve a converged solution is, respectively, smaller or larger than the prescribed (desired) number of iterations (which is set to 8 in our computations). If convergence cannot be achieved, the time increment is halved. The number of time steps needed to complete the simulation is thus an indicator of the robustness of the computational model (the smaller the number of time steps, the more robust the model, since the solution procedure can carry on with larger time increments).

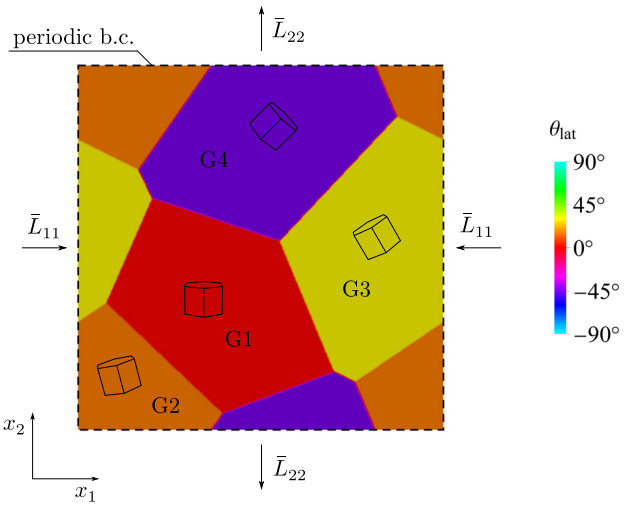

Fig. 3 Periodic four-grain unit cell: loading scheme and initial grain orientation

4 Study of performance and efficiency

In Sect. 4.1, we showcase the simulation results for a representative element type and mesh density. In Sect. 4.2, with the aim to evaluate the computational performance of the model, we report and discuss the simulation results for different element types and mesh densities. In Sect. 4.3, we investigate the sensitivity of the results and model's efficiency to the micromorphic regularization parameter ϵ_μ. Finally, in Sect. 4.4, we briefly examine the rate sensitivity effects.

4.1 Microstructure evolution in a periodic unit cell

The computational study reported below is carried out for a representative 2D problem of a periodic unit cell with four grains. The setup corresponds to the example studied in detail in Sect. 5.5 in [26]. Considering that the present study involves a large number of simulations, the computational cost has been reduced by employing a smaller unit cell with the size of 3×3 μm^2 containing four grains (instead of 5×5 μm^2 with 10 grains as in [26]) so that the grain size is approximately maintained. Otherwise, all material and process parameters are identical to those in [26]. The setup of the problem is briefly discussed below.

The unit cell under consideration is shown in Fig. 3. With reference to magnesium (HCP structure), a 2D plane-strain analysis is carried out within the $(\bar{1}2\bar{1}0)$ plane which is the shear plane of two conjugate twinning systems of the $\{10\bar{1}2\}\langle\bar{1}011\rangle$ family. As discussed in Sect. 2.2, the two conjugate twinning systems are represented by a single twin deformation variant, and accordingly by a single order parameter η and its micromorphic counterpart χ. Each grain is oriented differently. The grain orientation is characterized by the angle between the global x_2 axis and the local [0001]-axis (c axis). Specifically, grains G1, G2, G3 and G4 are set at angles 0°, 15°, 30°, and $-45°$ respectively, as illustrated in Fig. 3.

In addition to twinning, plastic slip on three slip systems is considered. One (easy) basal slip system with the (0001) slip plane and $[\bar{1}010]$ slip direction is considered, which is an equivalent slip system that represents two co-planar crystallographic basal slip systems with the $[\bar{2}110]$ and $[\bar{1}\bar{1}20]$ slip directions. Moreover, two symmetric equivalent (hard) pyramidal slip systems with the $(10\bar{1}1)$ and $(\bar{1}011)$ slip planes are considered, each representing two co-planar crystallographic $\langle a + c\rangle$ pyramidal slip systems.

Table 1 Material parameters

c_{11} [GPa]	c_{33} [GPa]	c_{12} [GPa]	c_{13} [GPa]	c_{44} [GPa]	γ_{tw} [-]	$\tau^{\text{c}}_{\text{tw}}$ [MPa]	$\tau^{\text{c}}_{\text{bas}}$ [MPa]	$\tau^{\text{c}}_{\text{pyr}}$ [MPa]	H [MPa]	Γ [J/m^2]	ℓ [nm]	ϵ_μ [GPa]	v_0 [nm/s]	$\dot{\gamma}_0$ [s^{-1}]
63.5	66.5	25.9	21.7	18.4	0.129	15	15	150	400	0.15	10	5	500	1

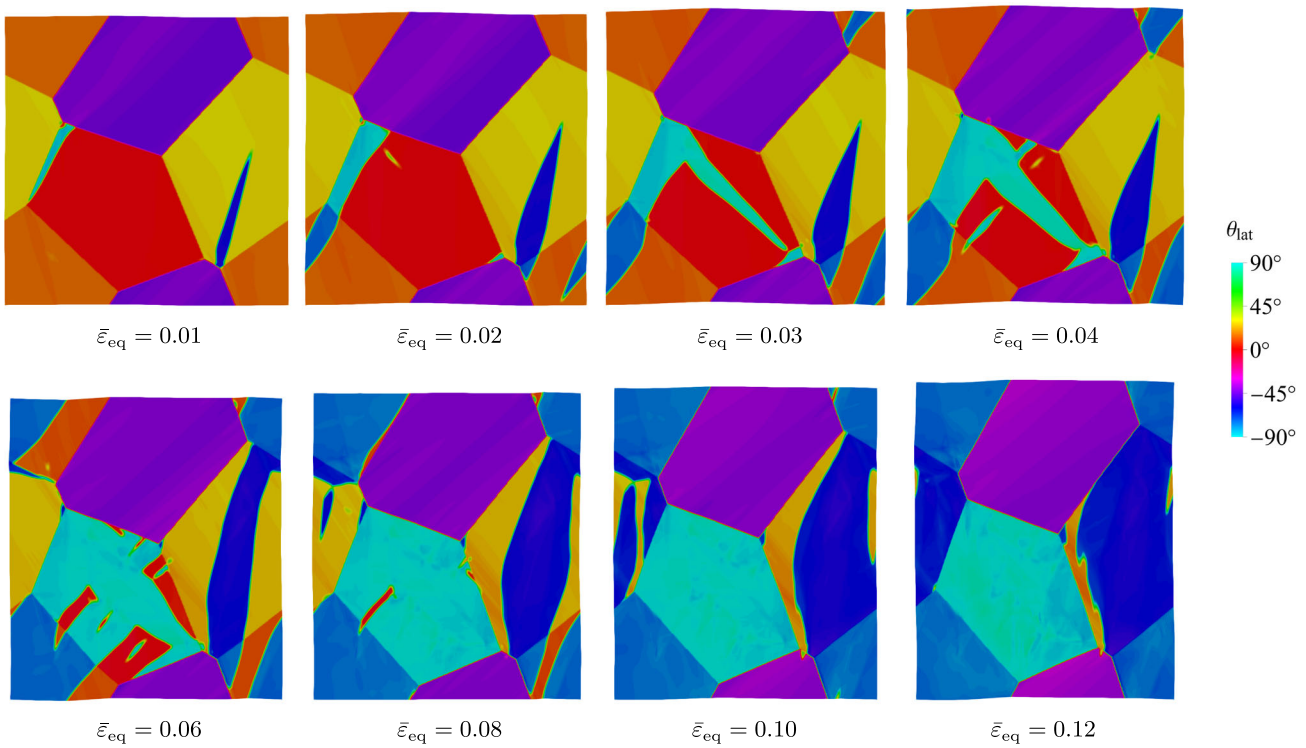

Fig. 4 Microstructure evolution in the four-grain unit cell during isochoric tension. Evolution of the local lattice orientation angle θ_{lat} is shown at selected values of the equivalent overall strain $\bar{\varepsilon}_{\text{eq}}$

The material parameters used in the simulations are provided in Table 1. Here, c_{ij} are the elastic constants, and $\tau^{\text{c}}_{\text{bas}}$ and $\tau^{\text{c}}_{\text{pyr}}$ denote the critical resolved shear stresses (equal for the matrix and for the twin) for the basal and pyramidal slip systems, respectively. For the c/a ratio of 1.624, the value typical for magnesium, the twinning shear is $\gamma_{\text{tw}} = 0.129$. See [26] for the references and additional comments on the selection of the parameter values.

The unit cell is subjected to isochoric tension along the x_2-axis. This is accomplished by prescribing a constant overall (macroscopic) velocity gradient $\bar{\mathbf{L}} = \dot{\bar{\mathbf{F}}}\bar{\mathbf{F}}^{-1}$ in the form,

$$\bar{\mathbf{L}} = \frac{\sqrt{3}}{2}\bar{d}\begin{pmatrix} -1 & 0 \\ 0 & 1 \end{pmatrix}, \tag{81}$$

where $\bar{d} = 0.01\ \text{s}^{-1}$. At the same time, periodic boundary conditions are enforced (using Lagrange multipliers) on the displacement field (periodicity of the displacement fluctuation) and on the micromorphic variable χ. Since twins in each grain are independent, a separate field of the micromorphic variable is defined for each grain with the homogeneous natural boundary condition enforced on the grain boundaries. Note that a regular mesh of quadrilateral elements is used (see the next section for details), so that the grain boundaries have a step-like appearance.

To illustrate the microstructure evolution due to coupled twinning and plastic slip, Fig. 4 shows a series of snapshots of the local lattice orientation angle θ_{lat} that is defined as the angle between the global x_2-axis and the local c axis (the orientation angle θ_{lat} is represented by a 180°-periodic color scale). The individual snapshots are labeled by the equivalent overall strain $\bar{\varepsilon}_{\text{eq}} = (\frac{2}{3}\bar{\boldsymbol{H}} \cdot \bar{\boldsymbol{H}})^{1/2}$ which is defined in terms of the overall logarithmic strain $\bar{\boldsymbol{H}}$. Since twinning is associated with a rotation by 90° ± 3.7°, the distribution of θ_{lat} clearly depicts the progress of the twinning transformation. The results are here reported for the Q2sH1-R element and for the finest mesh considered.

Figure 5 illustrates the inhomogeneity of deformation and stress within the unit cell and within the individual grains. In addition to the lattice orientation angle θ_{lat} (selected

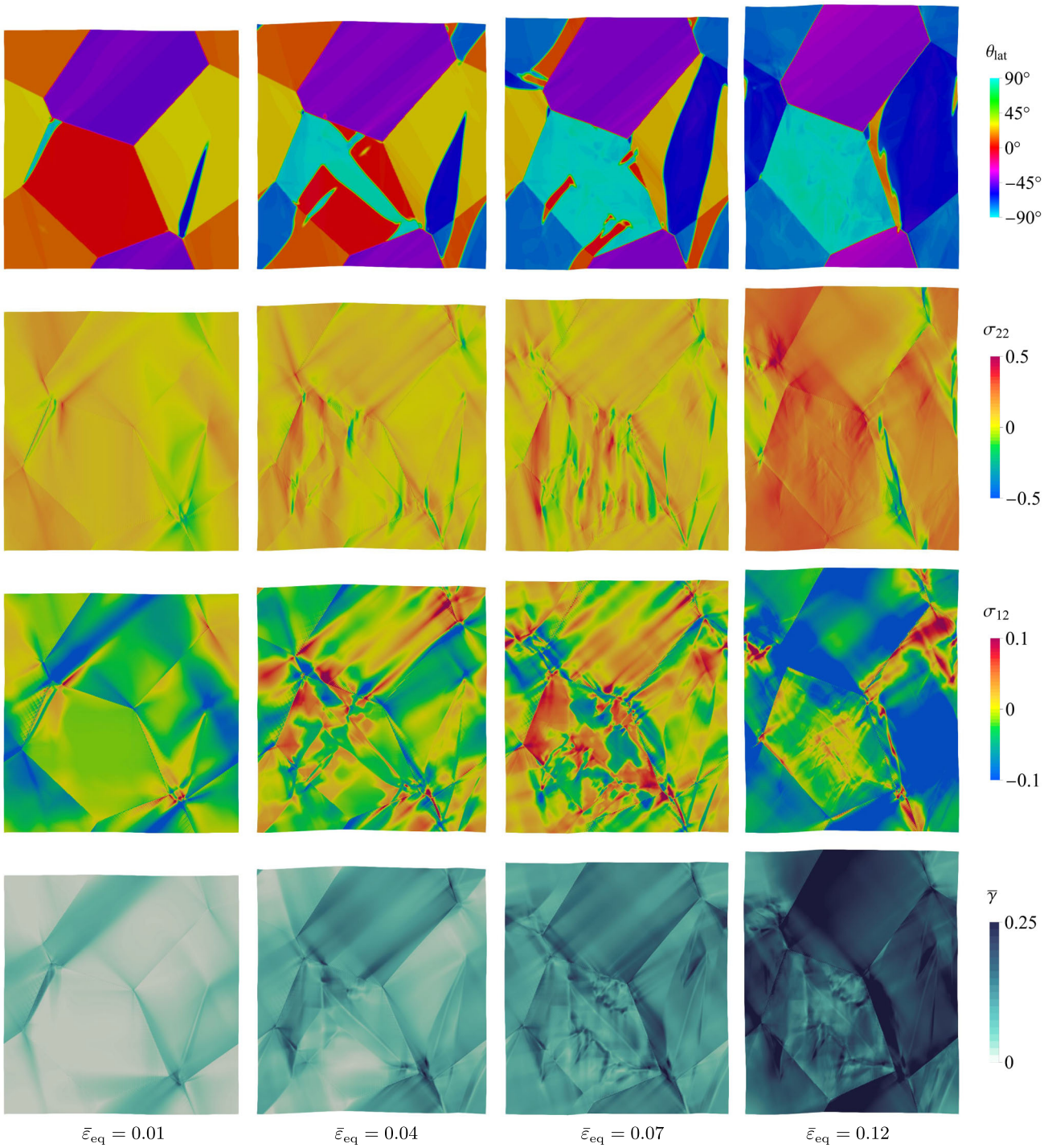

Fig. 5 Inhomogeneity of deformation illustrated by (from the top): lattice orientation angle θ_{lat}, Cauchy stress components σ_{22} and σ_{12}, and accumulated plastic slip $\bar{\gamma}$ at selected stages of deformation

snapshots from Fig. 4), shown is the distribution of the accumulated plastic slip $\bar{\gamma}$ and two components of the Cauchy stress $\boldsymbol{\sigma}$. While inhomogeneity of plastic deformation in a polycrystalline aggregate is a well-known phenomenon, microstructure evolution due to twinning is here an additional contribution, and this is captured by the spatially-resolved modeling using the phase-field method. In fact, deformation twinning leads to a severe inhomogeneity in the microstructure. This can be observed not only directly in the grains undergoing twin transformation, such as grain G1 in which the interaction between plastic slip and twinning intensifies the microstructure inhomogeneity, but also in the neighbor-

Table 2 The total number of elements, displacement nodes and degrees of freedom for six mesh densities (MD1 to MD6) and all element types considered, cf. Fig. 2

	No. of elements	MD1 4900	MD2 10,000	MD3 19,600	MD4 40,000	MD5 78,400	MD6 160,000
Q1H1(-Fbar)	No. of nodes	5,041	10,201	19,881	40,401	78,961	160,801
	No. of d.o.f	15,919	31,736	61,223	123,457	240,033	486,900
Q2sH1(-R)	No. of nodes	14,981	30,401	59,361	120,801	236,321	481,601
	No. of d.o.f	36,079	72,536	140,743	285,057	555,873	1,130,100
Q2H1	No. of nodes	19,881	40,401	78,961	160,801	314,721	641,601
	No. of d.o.f	45,879	92,536	179,943	365,057	712,673	1,450,100
Q2sH2s(-R)	No. of nodes	14,981	30,401	59,361	120,801	236,321	481,601
	No. of d.o.f	46,668	93,662	181,516	367,304	715,816	1,454,590
Q2H2	No. of nodes	19,881	40,401	78,961	160,801	314,721	641,601
	No. of d.o.f	61,368	123,662	240,316	487,304	951,016	1,934,590

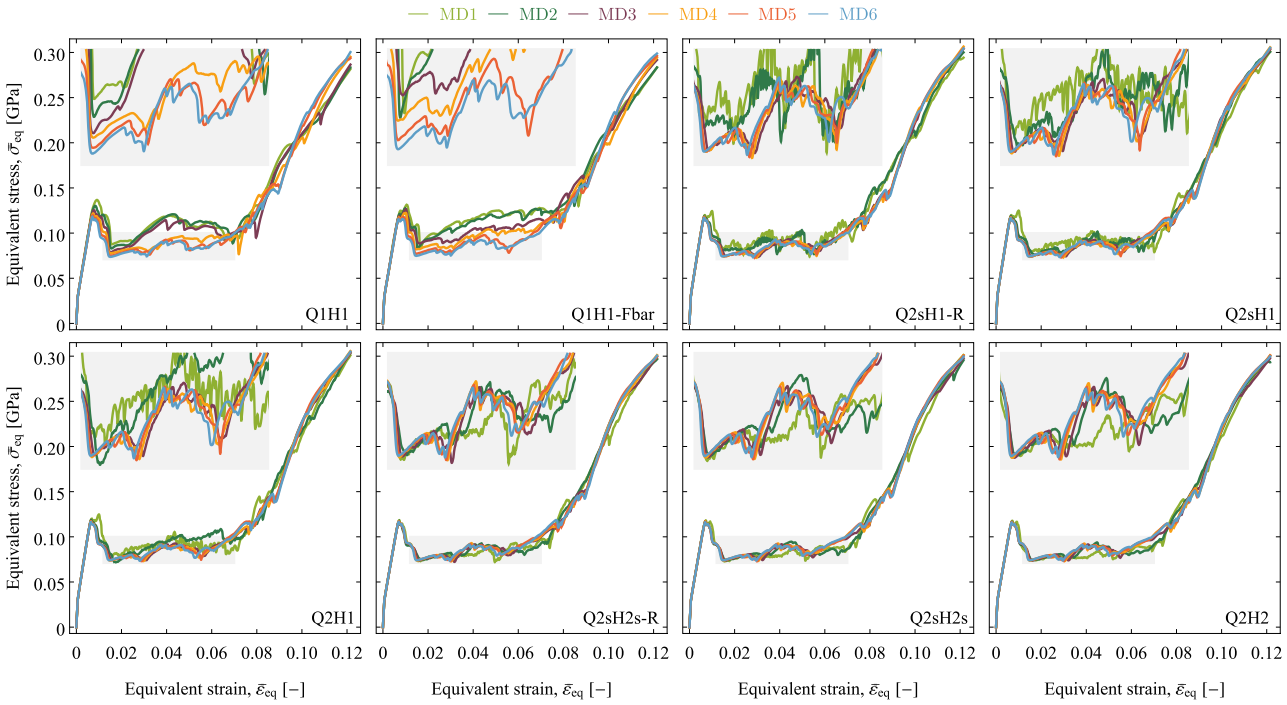

Fig. 6 Effect of element type and mesh density on the macroscopic stress–strain response represented by the equivalent stress $\bar{\sigma}_{eq}$ as a function of the equivalent strain $\bar{\varepsilon}_{eq}$. Each panel corresponds to the element type indicated in the bottom-right corner. The shaded areas are enlarged in the insets

ing grain, i.e., grain G4 with no twin transformation, where a visible inhomogeneous deformation is induced as a result of twin impinging at the grain boundary.

4.2 Effect of element type and mesh density

A detailed study of the effect of element type and mesh density on the performance of the computational model is carried out in this section. To this end, a set of six regular finite-element meshes of increasing density is considered starting from a coarse mesh of 70×70 elements (MD1, element size $h = 43\,\text{nm}$) to the finest mesh of 400×400 elements (MD6, $h = 7.5\,\text{nm}$). Table 2 provides the number of displacement nodes and the number of degrees of freedom (see Fig. 2) for each mesh density and for each element type.

Figures 6 and 7 depict the macroscopic response obtained for all elements and all mesh densities. The response is provided in terms of the equivalent macroscopic stress $\bar{\sigma}_{eq} = (\frac{3}{2}\bar{\mathbf{s}}\cdot\bar{\mathbf{s}})^{1/2}$, where $\bar{\mathbf{s}}$ is the deviator of the macroscopic Cauchy stress $\bar{\boldsymbol{\sigma}}$, as a function of the equivalent macroscopic strain $\bar{\varepsilon}_{eq}$. Enlarged views of the plateaus are shown in the insets. Each panel in Fig. 6 corresponds to one of the element types and includes the equivalent stress–strain curves obtained for all six mesh densities. On the other hand, each panel in Fig. 7 corresponds to a selected mesh density and includes the curves obtained for all element types.

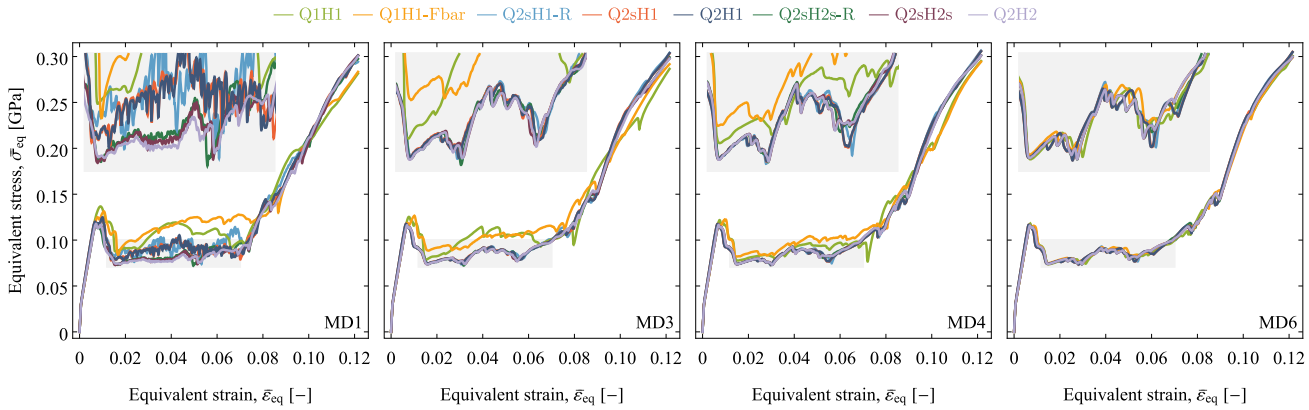

Fig. 7 Effect of element type and mesh density on the macroscopic stress–strain ($\bar{\sigma}_{eq}$–$\bar{\varepsilon}_{eq}$) response. Each panel corresponds to the mesh density indicated in the bottom-right corner. The shaded areas are enlarged in the insets

The first observation from Figs. 6 and 7 is that, with mesh refinement, all responses converge to (nearly) the same outcome. The converged response is characterized by several stress drops that are associated with abrupt events, mostly nucleation of twins. The first stress peak and the subsequent largest stress drop at $\bar{\varepsilon}_{eq} \approx 0.01$ are associated with the first two twins that appear in grains G1 and G3, see the first snapshot in Fig. 4. After this first stress drop, the deformation is characterized by a stress plateau with much weaker stress drops that accompany further evolution of the twin microstructure, cf. Fig. 4. After the plateau, say at $\bar{\varepsilon}_{eq} \approx 0.07$, a hardening stage can be observed which is associated with activation of hard pyramidal slip systems as a result of saturation of twinning (all grains are fully twinned except grain G4 which is oriented unfavorably and does not twin at all).

As indicated above, the stress drops correspond to abrupt microstructure evolution events, hence the pattern of the irregularities in the stress–strain response is, in fact, a kind of representation (a fingerprint) of the underlying microstructure evolution. Accordingly, the same sequence of stress drops in two stress–strain responses suggests that they correspond to the same sequence of microstructure evolution events. This is confirmed by Fig. 8 which compares the microstructure represented by the lattice orientation angle θ_{lat} at $\bar{\varepsilon}_{eq} = 0.04$ and at $\bar{\varepsilon}_{eq} = 0.08$ for all elements and for three selected mesh densities. For the finest mesh (MD=6), only very minor differences can be seen, which is consistent with the corresponding converged stress–strain response obtained for all elements, as shown in Fig. 7. On the other hand, differences in the microstructures obtained for the coarsest mesh (MD1) are visible, see, e.g., grain G1 at $\bar{\varepsilon}_{eq} = 0.04$ and grain G3 at $\bar{\varepsilon}_{eq} = 0.08$. Here, the differences arise not only among the element types but also in comparison to the microstructure obtained for the finest mesh (MD6). For the intermediate mesh density (MD3), only the microstructures predicted by the low-order elements (Q1H1 and Q1H1-Fbar) are inconsistent with the microstructure of the finest mesh, while those predicted by the remaining elements are in a reasonable agreement with it.

Figures 6, 7, and 8 consistently show that the convergence with mesh refinement is visibly poorer in the case of the two low-order elements (Q1H1 and Q1H1-Fbar). It follows from Fig. 6 that in both cases a correct sequence of the microstructure evolution events is obtained only for the two finest meshes (MD5 and MD6). In the case of the remaining elements (Q2 and Q2s displacement interpolation), the sequence of the events is represented with a reasonable accuracy already for MD3. Of course, for the same mesh density, the low-order elements have a smaller number of degrees of freedom, hence a direct comparison of the overall computational efficiency is not straightforward, as discussed below.

The computational cost is illustrated in Fig. 9 which shows the total wall-clock time as a function of the number of degrees of freedom, as well as its two ingredients, namely the total linear-solver time and the total assembly time, the latter involving mostly the computation of element quantities (element contributions to the residual vector and tangent matrix). Note that, in each case (element type and mesh density), the simulation has been completed with a different total number of time steps, see Fig. 10, as a result of the adaptive time incrementation algorithm employed.

The numbers reported in Fig. 9 concern the total computational cost. Each computation time is the product of the respective cost of one Newton iteration and the total number of iterations, while the total number of iterations is roughly proportional to the number of time steps. The cost of one Newton iteration is approximately constant for a fixed element type and mesh density and depends on various factors. For instance, the assembly time per iteration is proportional to the number of Gauss points and is thus lower for the quadratic elements with reduced integration (Q2sH1-R, Q2sH2s-R) than for the fully integrated quadratic elements. The linear-

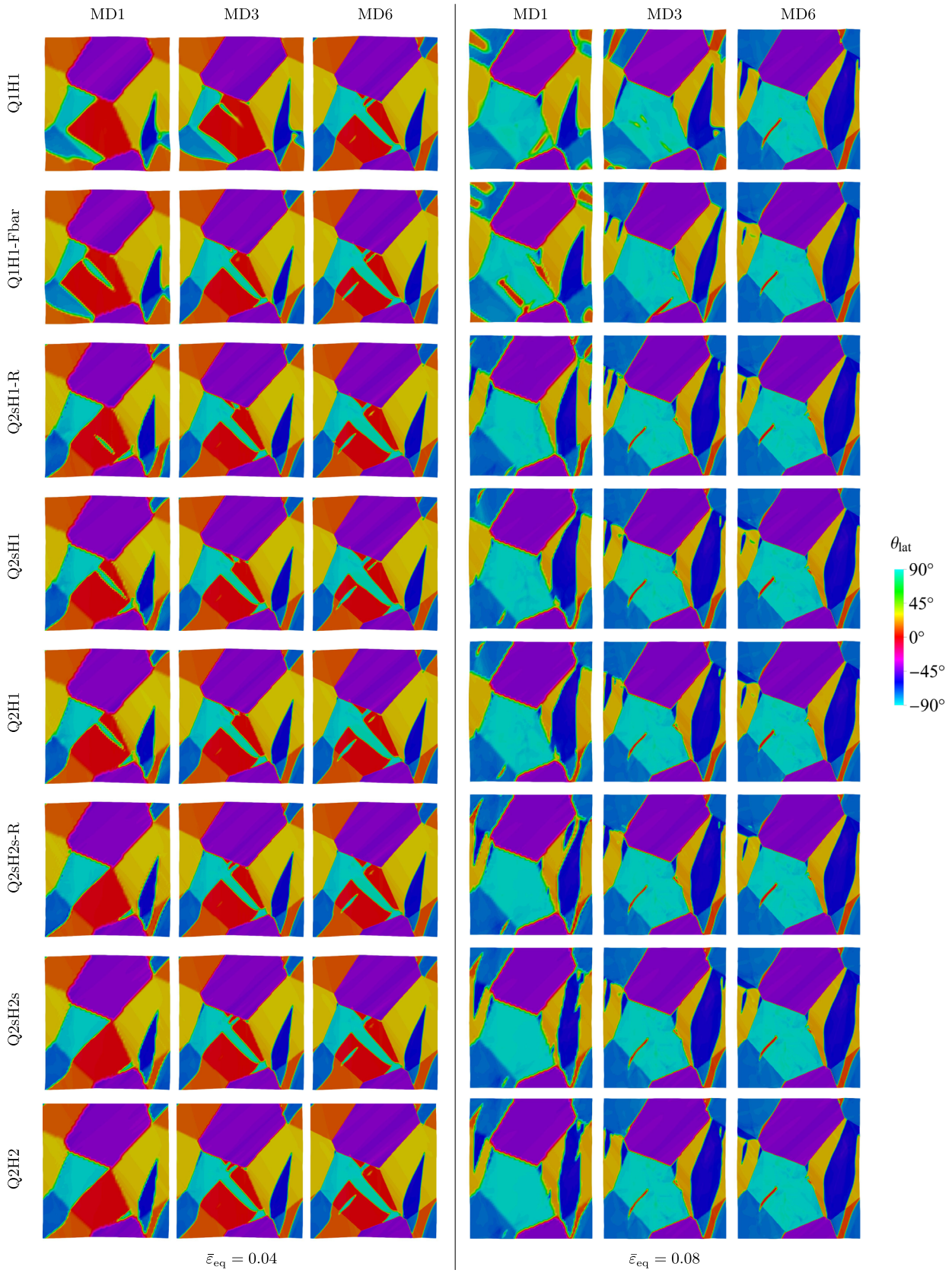

Fig. 8 Comparison of the microstructure obtained for all element types and for three selected mesh densities (MD1, MD3, MD6) at two representative stages of deformation ($\bar{\varepsilon}_{eq} = 0.04$ and $\bar{\varepsilon}_{eq} = 0.08$)

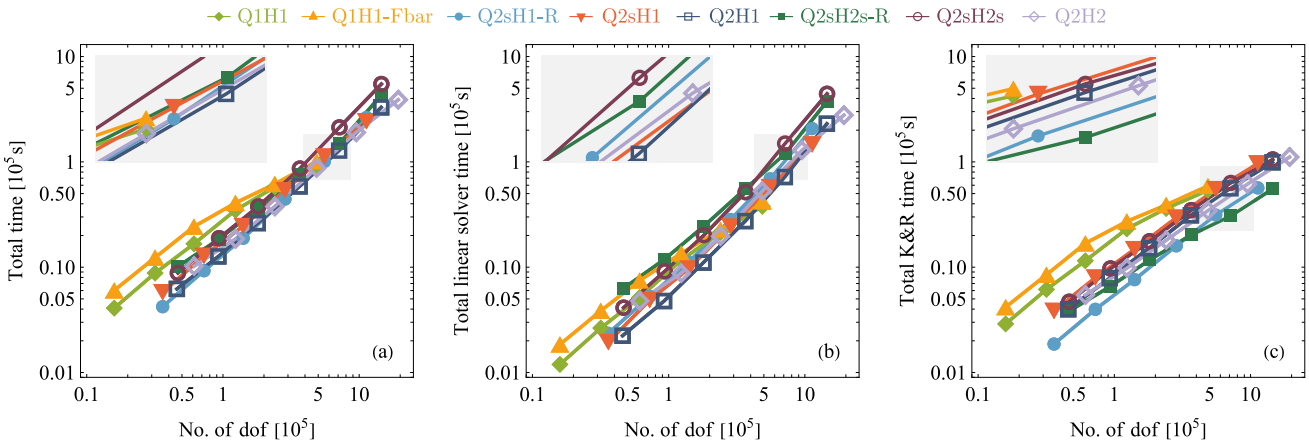

Fig. 9 Computational efficiency: **a** the total wall-clock time, **b** linear-solver time and **c** assembly time as a function of the total number of degrees of freedom

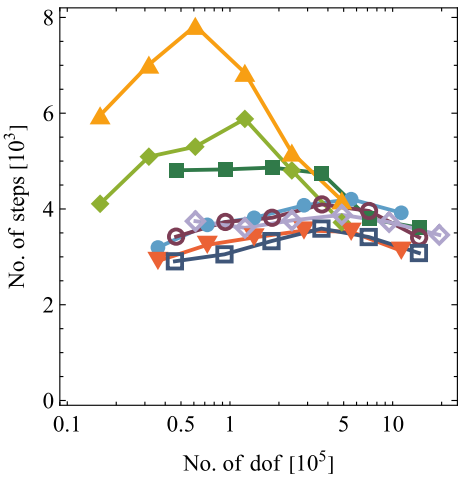

Fig. 10 Robustness: the number of time steps needed to complete the simulation (an adaptive time incrementation algorithm is used) as a function of the total number of degrees of freedom. The line legend is provided in Fig. 9

solver time naturally depends on the number of degrees of freedom, but it may also be affected by the sparsity of the tangent matrix, etc.

From Fig. 10 it follows that the robustness of the computational model with different element types varies significantly. At the same time, overall, the differences in the total computational cost are visible, but not large, see Fig. 9a, particularly for higher mesh densities that deliver reliable results in terms of both microstructure evolution and stress–strain response. Elements Q2sH1-R and Q2H1 appear to be the most efficient, except for the finest mesh (MD6), for which element Q2H2 is characterized by a slightly lower cost. Of course, the above comparison is specific to the details of the computational scheme outlined in Sect. 3.5.

In the above study, the element size has been varied between $h = 43\,\text{nm}$ for MD1 and $h = 7.5\,\text{nm}$ for MD6. It follows that for $\ell = 10\,\text{nm}$, as used in all computations, the ratio of ℓ to h ranges from $\ell/h = 0.23$ for MD1 to $\ell/h = 1.33$ for MD6. Considering that the theoretical thickness of the diffuse interface is $\pi\ell$ [39, 40], this corresponds to $\pi\ell/h = 0.73$ for MD1 and $\pi\ell/h = 4.19$ for MD6. Earlier studies suggest that at least 3–4 elements per interface thickness are needed to accurately resolve the profile of the diffuse interface [22, 27], although this condition concerns piecewise-linear approximation of the order parameter (i.e., H1 elements in the present study), and this ratio is expected to be smaller for quadratic (H2s and H2) elements. Clearly, the above condition is satisfied only for the finest meshes used in the present study. However, as discussed above, acceptable results can be obtained also for the meshes that would be considered too coarse according to the above condition. The good performance of the present model for the meshes that seem to be too coarse may be attributed to the micromorphic formulation, Eqs. (15) and (16). More specifically, as a result of the penalty regularization, an additional diffuseness of the interface is introduced which provides a kind of a regularization to the problem at hand.

4.3 Effect of the micromorphic regularization

In this section, we study the effect of the micromorphic penalty parameter ϵ_μ on the response and robustness of the model. The results reported above correspond to $\epsilon_\mu = 5\,\text{GPa}$, the value used in our previous work [26] and selected based on theoretical considerations and prior experience [42, 55]. Here, parameter ϵ_μ is varied in a wide range between 0.05 and 50 GPa, and the corresponding results are reported below for the element Q2sH1-R and for the mesh density varied between MD2 and MD5. Note that this element was used in our previous study [26] and exhibited a good performance, which is also corroborated here, as shown in Sect. 4.2.

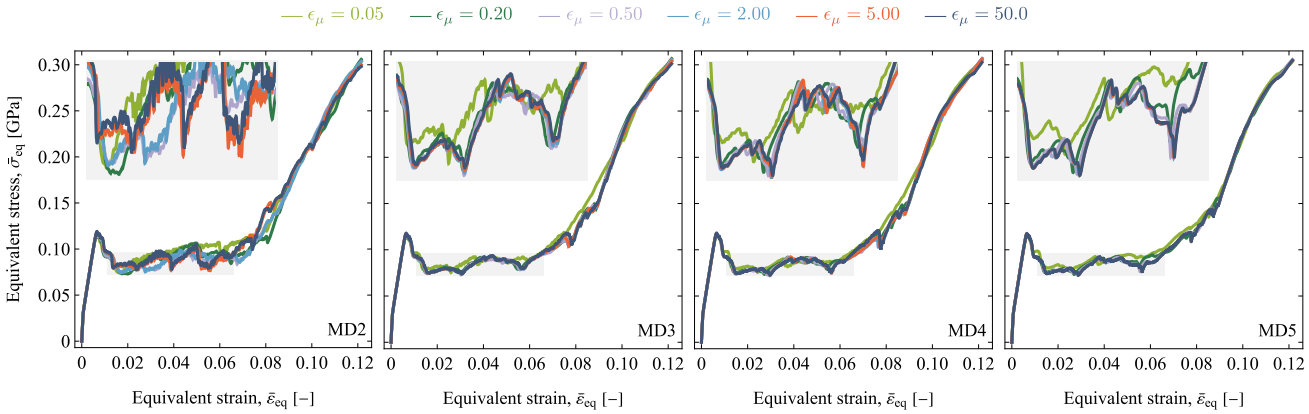

Fig. 11 Effect of the micromorphic penalty parameter ϵ_μ on the macroscopic stress–strain response ($\bar{\sigma}_{eq}$–$\bar{\varepsilon}_{eq}$) for selected mesh densities

Figure 11 shows the effect of ϵ_μ on the macroscopic stress–strain response. It can be seen that, for $\epsilon_\mu = 0.5\,\text{GPa}$ and higher, the response is practically insensitive to ϵ_μ, except for the coarse mesh (MD2). As discussed in Sect. 4.2, a good agreement of the fine features of the stress–strain response indicates that also the microstructure evolution proceeds along a similar path, and this is illustrated in Fig. 12. Compared to higher values of ϵ_μ, small differences in the microstructure can be seen for $\epsilon_\mu = 0.05\,\text{GPa}$, while those for $\epsilon_\mu = 0.5\,\text{GPa}$ and $5\,\text{GPa}$ are practically identical, except for the coarse mesh (MD2) which is too coarse to deliver a correct microstructure regardless of the value of ϵ_μ. Increasing ϵ_μ to $50\,\text{GPa}$ does not affect the microstructure (not included in Fig. 12), while the computational cost increases significantly.

Figure 13 shows the effect of the micromorphic penalty parameter on the number of time steps needed to complete the simulation. Recall that an adaptive time incrementation algorithm is used, and the computational cost is directly proportional to the number of time steps. It follows that for all mesh densities the number of time steps is the lowest for $\epsilon_\mu = 0.5\,\text{GPa}$. This value seems thus to be optimal in terms of efficiency, especially considering its ability to yield reasonably accurate results, as discussed above. Note, however, that somewhat higher values of ϵ_μ may be preferable to guarantee a higher accuracy, at the expense of a slightly higher computational cost, as for $\epsilon_\mu = 2\,\text{GPa}$. Interestingly, for $\epsilon_\mu = 2\,\text{GPa}$, the number of time steps is practically insensitive to the mesh density.

4.4 Rate sensitivity

The form of the dissipation potential D, Eqs. (20)–(22), specifies the evolution equations in the form of Perzyna-type overstress model with linear viscosity, see Eq. (31). As discussed in Sect. 2.4, the loading rate—here specified by the overall strain rate $\bar{d}$, see Eq. (81)—is adopted such that the corresponding rate-effects are not much pronounced. This is illustrated in Fig. 14 which shows the macroscopic stress–strain response for the overall strain rate $\bar{d}$ varied between $0.001\ \text{s}^{-1}$ and $0.1\ \text{s}^{-1}$ (the reference value used in the preceding computations is $\bar{d} = 0.01\ \text{s}^{-1}$). Note that the rate effects could be equivalently examined by scaling the reference slip rate $\dot{\gamma}_0$ and reference interface propagation speed v_0. The results are reported here for the element Q2sH1-R and for two representative mesh densities (MD3, MD4).

It follows from Fig. 14 that indeed the stress–strain response does not change significantly when the overall strain rate $\bar{d}$ is decreased from the reference value of $0.01\ \text{s}^{-1}$ to $0.001\ \text{s}^{-1}$, particularly for the finer mesh MD4. Also, the twin microstructure that develops during deformation shows very minor differences (the corresponding results are thus not shown). On the other hand, when $\bar{d}$ is increased to $0.03\ \text{s}^{-1}$ and to $0.1\ \text{s}^{-1}$, significant changes in the stress–strain response are observed, and those changes are accompanied by visible changes in the twin microstructure (not shown). This confirms our earlier observation that the overall stress–strain response may serve as a fingerprint of the underlying microstructure evolution.

Figure 15 shows the total number of time steps as a function of the overall strain rate $\bar{d}$. Note that, for a given element type and mesh density, the computational cost (the total wall-clock time) is proportional to the number of time steps, hence the number of time steps can be used as a measure of computational efficiency. As expected, when $\bar{d}$ is decreased, the number of time steps increases so that the use of the viscous regularization is associated with the common efficiency–accuracy trade-off. Overall, the results in Figs. 14 and 15 indicate that the rate effects in our main simulations are mild, and reduction of those effects would lead to an increase in computational cost.

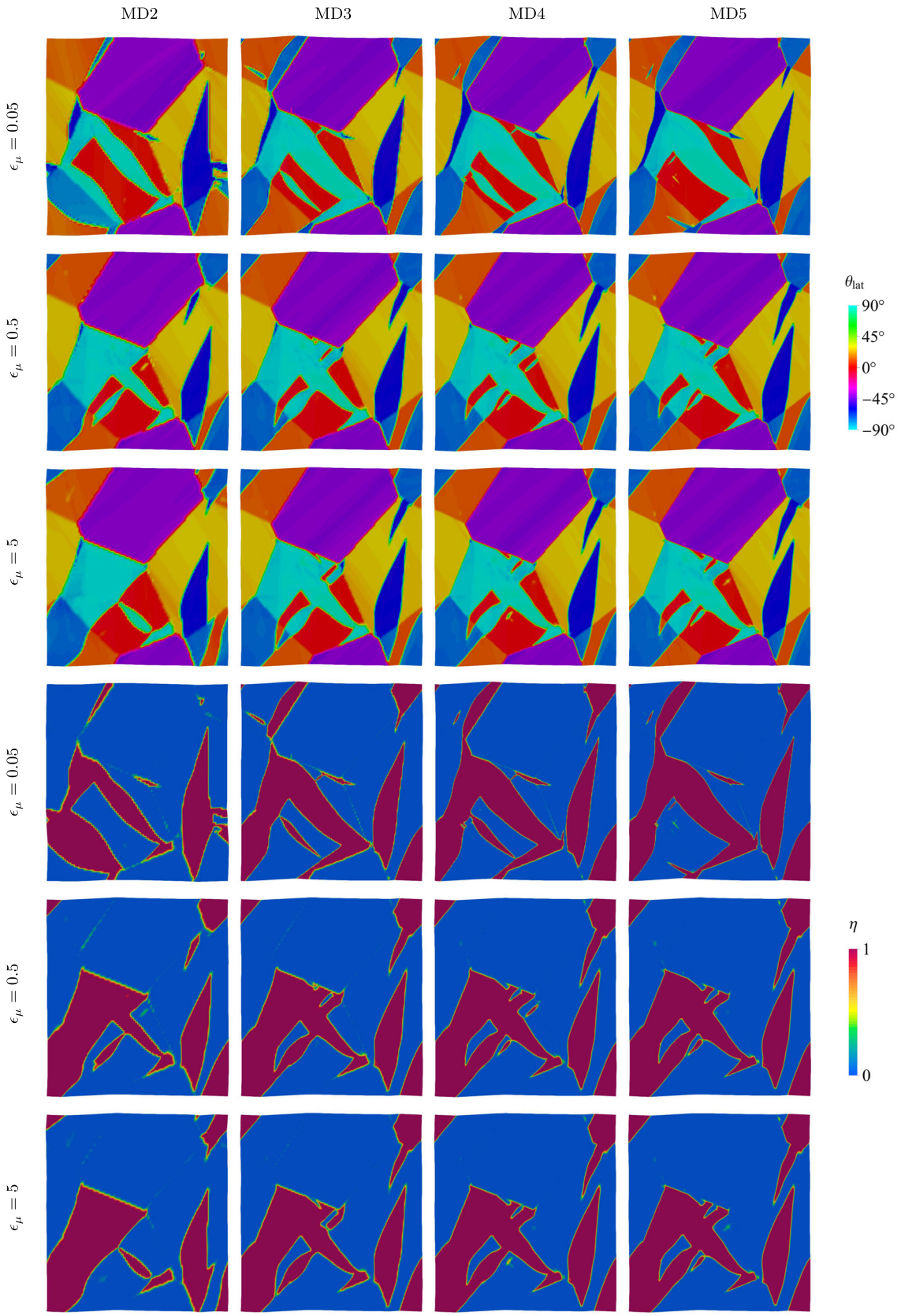

Fig. 12 Comparison of the microstructure at $\bar{\varepsilon}_{\text{eq}} = 0.05$ obtained for three values of the micromorphic penalty parameter $\epsilon_\mu = \{0.05, 0.5, 5\}$ GPa and for four mesh densities (MD2, MD3, MD4 and MD5): lattice orientation angle θ_{lat} (top) and order parameter η (bottom)

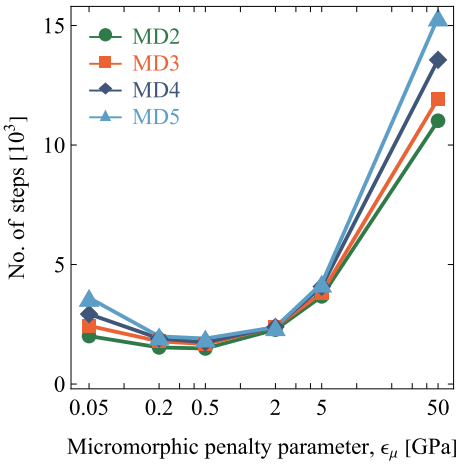

Fig. 13 The total number of time steps as a function of the micromorphic penalty parameter ϵ_μ

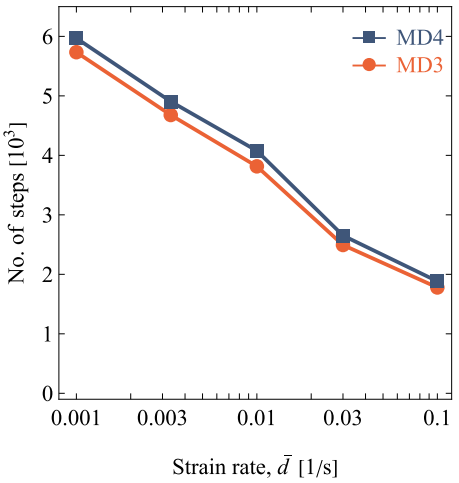

Fig. 15 The total number of time steps as a function of the overall strain rate $\bar{d}$

5 Conclusion

A comprehensive numerical study has been carried out to assess the computational performance of the phase-field model of coupled deformation twinning and crystal plasticity. The model was first presented in [26] where its capability in capturing the evolution of the twin microstructure was shown. In this paper, the specific issues addressed are the incremental formulation and computational treatment of the model, as well as the model's efficiency with regard to the choice of elements in the finite-element discretization, mesh density, and micromorphic regularization parameter. A series of 2D simulations have been performed for a periodic unit cell containing four grains, leading to several key observations:

- For the finest mesh density, all the element types converge to practically the same solution.
- Despite coarse meshes fail to capture the details of the microstructure and mechanical response, which is especially evident for low-order discretizations (Q1H1 and Q1H1-Fbar), the produced results maintain reasonable qualitative resemblance to those from finer mesh densities.
- Low-order elements display the largest variation in computational efficiency as a function of mesh density. As the mesh becomes finer, different element types yield similar robustness. Overall, the computational study indicates that Q2sH1-R and Q2H1 element types exhibit the superior efficiency.

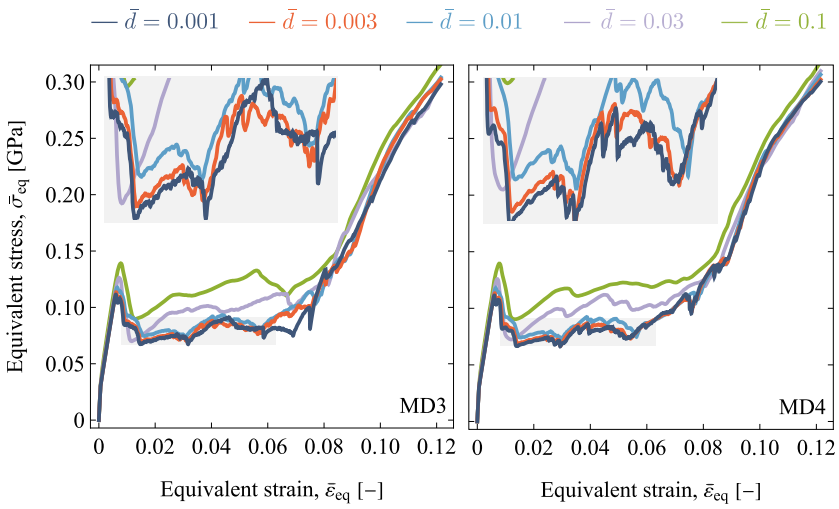

Fig. 14 Effect of the overall strain rate $\bar{d}$ on the macroscopic stress–strain response ($\bar{\sigma}_{\text{eq}}$–$\bar{\varepsilon}_{\text{eq}}$)

- The sensitivity of the simulation results to the micromorphic regularization parameter ϵ_μ suggests that coarser meshes are more susceptible to the changes in ϵ_μ. The corresponding study of computational efficiency highlights two characteristic points: one at $\epsilon_\mu = 0.5$ GPa, demonstrating the optimal performance and results of acceptable quality, and the other at $\epsilon_\mu = 2$ GPa, where no discernible change in robustness is visible across different mesh densities.
- The rate sensitivity analysis confirms that our simulation results are not markedly influenced by rate effects.

Acknowledgements PS and SS have been partially supported by the National Science Centre (NCN) in Poland through Grant No. 2018/29/B/ST8/00729. MRH acknowledges the support from the National Science Centre (NCN) in Poland through the Grant No. 2021/43/D/ST8/02555. For the purpose of Open Access, the authors have applied a CC-BY public copyright license to any Author Accepted Manuscript (AAM) version arising from this submission.

References

1. Chen LQ (1995) A novel computer simulation for modeling grain growth. Scr Metall Mater 32(1):115–120
2. Steinbach I, Pezzolla F, Nestler B, Seeßelberg M, Prieler R, Schmitz G, Rezende J (1996) A phase field concept for multiphase systems. Phys. D 94:135–147
3. Moelans N, Blanpain B, Wollants P (2006) Phase field simulations of grain growth in two-dimensional systems containing finely dispersed second-phase particles. Acta Mater 54:1175–1184
4. Dantzig JA, Di Napoli P, Friedli J, Rappaz M (2013) Dendritic growth morphologies in Al-Zn alloys-Part II: Phase-field computations. Metall. Mat. Trans. A 44:5532–5543
5. Takaki T, Sakane S, Ohno M, Shibuta Y, Shimokawabe T, Aoki T (2016) Primary arm array during directional solidification of a single-crystal binary alloy: Large-scale phase-field study. Acta Mater 118:230–243
6. Wang Y, Khachaturyan AG (1997) Three-dimensional field model and computer modeling of martensitic transformations. Acta Mater 45:759–773
7. Levitas VI, Levin VA, Zingerman KM, Freiman EI (2009) Displacive phase transitions at large strains: phase-field theory and simulations. Phys Rev Lett 103:025702
8. Zhong Y, Zhu T (2014) Phase-field modeling of martensitic microstructure in NiTi shape memory alloys. Acta Mater 75:337–347
9. Tůma K, Stupkiewicz S, Petryk H (2016) Size effects in martensitic microstructures: finite-strain phase field model versus sharp-interface approach. J Mech Phys Solids 95:284–307
10. Chen LQ (2008) Phase-field method of phase transitions/domain structures in ferroelectric thin films: a review. J Am Ceram Soc 91:1835–1844
11. Schrade D, Müller R, Gross D, Keip MA, Thai H, Schröder J (2014) An invariant formulation for phase field models in ferroelectrics. Int J Solids Struct 51:2144–2156
12. Reichel M, Xu BX, Schröder J (2022) A comparative study of finite element schemes for micromagnetic mechanically coupled simulations. J Appl Phys 132:183903
13. Guin L, Kochmann DM (2023) A phase-field model for ferroelectrics with general kinetics, part I: model formulation. J Mech Phys Solids 176:105301
14. Tourret D, Liu H, LLorca J (2022) Phase-field modeling of microstructure evolution: recent applications, perspectives and challenges. Prog Mater Sci 123:100810
15. Penrose O, Fife PC (1990) Thermodynamically consistent models of phase-field type for the kinetic of phase transitions. Phys D 43:44–62
16. Finel A, Le Bouar Y, Dabas B, Appolaire B, Yamada Y, Mohri T (2018) Sharp phase field method. Phys Rev Lett 121:025501
17. Fleck M, Schleifer F (2023) Sharp phase-field modeling of isotropic solidification with a super efficient spatial resolution. Eng Comput 39(3):1699–1709
18. Lo YS, Hughes TJR, Landis CM (2023) Phase-field fracture modeling for large structures. J Mech Phys Solids 171:105118
19. Dobrzański J, Stupkiewicz S (2024) Towards a sharper phase-field method: a hybrid diffuse-semisharp approach for microstructure evolution problems. Comput Methods Appl Mech Eng 423:116841
20. Kochmann J, Wulfinghoff S, Reese S, Rezaei Mianroodi J, Svendsen B (2016) Two-scale FE-FFT-and phase-field-based computational modeling of bulk microstructural evolution and macroscopic material behavior. Comput Methods Appl Mech Eng 305:89–110
21. DeWitt S, Rudraraju S, Montiel D, Andrews WB, Thornton K (2020) PRISMS-PF: a general framework for phase-field modeling with a matrix-free finite element method. npj Comput Mater 6:29
22. Tůma K, Rezaee-Hajidehi M, Hron J, Farrell PE, Stupkiewicz S (2021) Phase-field modeling of multivariant martensitic transformation at finite-strain: computational aspects and large-scale finite-element simulations. Comput Methods Appl Mech Eng 377:113705
23. Kondo R, Tadano Y, Shizawa K (2014) A phase-field model of twinning and detwinning coupled with dislocation-based crystal plasticity for HCP metals. Comput Mater Sci 95:672–683
24. Hu X, Ji Y, Chen L, Lebensohn RA, Chen LQ, Cui X (2021) Spectral phase-field model of deformation twinning and plastic deformation. Int J Plast 143:103019
25. Liu C, Roters F, Raabe D (2023) Finite strain crystal plasticity-phase field modeling of twin, dislocation, and grain boundary interaction in hexagonal materials. Acta Mater 242:118444
26. Rezaee-Hajidehi M, Sadowski P, Stupkiewicz S (2022) Deformation twinning as a displacive transformation: finite-strain phase-field model of coupled twinning and crystal plasticity. J Mech Phys Solids 163:104855
27. Levitas VI, Javanbakht M (2011) Phase-field approach to martensitic phase transformations: effect of martensite-martensite interface energy. Int. J. Mat. Res. 102(6):652–665
28. Ammar K, Appolaire B, Cailletaud G, Forest S (2009) Combining phase field approach and homogenization methods for modelling phase transformation in elastoplastic media. Eur J Comput Mech 18:485–523
29. Mosler J, Shchyglo O, Montazer Hojjat H (2014) A novel homogenization method for phase field approaches based on partial rank-one relaxation. J Mech Phys Solids 68:251–266

30. Schneider D, Tschukin O, Choudhury A, Selzer M, Böhlke T, Nestler B (2015) Phase-field elasticity model based on mechanical jump conditions. Comput Mech 55:887–901
31. Kiefer B, Furlan T, Mosler J (2017) A numerical convergence study regarding homogenization assumptions in phase field modeling. Int J Num Methods Eng 112:1097–1128
32. Sarhil M, Shchyglo O, Brands D, Schröder J, Steinbach I (2023) Modeling martensitic transformation in shape memory alloys using multi-phase-field elasticity models based on partial rank-one energy relaxation on pairwise interfaces. https://doi.org/10.48550/arXiv.2304.02406
33. Scherer JM, Phalke V, Besson J, Forest S, Hure J, Tanguy B (2020) Lagrange multiplier based vs micromorphic gradient-enhanced rate-(in)dependent crystal plasticity modelling and simulation. Comput Methods Appl Mech Eng 372:113426
34. Christian JW, Mahajan S (1995) Deformation twinning. Prog Mater Sci 39:1–157
35. Liu H, Lin FX, Zhao P, Moelans N, Wang Y, Nie JF (2018) Formation and autocatalytic nucleation of co-zone $\{10\bar{1}2\}$ deformation twins in polycrystalline Mg: a phase field simulation study. Acta Mater 153:86–107
36. Bruzy N, Denoual C, Vattré A (2022) Polyphase crystal plasticity for high strain rate: Application to twinning and retwinning in tantalum. J Mech Phys Solids 166:104921
37. Schröder J, Neff P (2003) Invariant formulation of hyperelastic transverse isotropy based on polyconvex free energy functions. Int J Solids Struct 40:401–445
38. Schröder J, Neff P, Ebbing V (2008) Anisotropic polyconvex energies on the basis of crystallographic motivated structural tensors. J Mech Phys Solids 56:3486–3506
39. Steinbach I (2009) Phase-field models in materials science. Model Simul Mater Sci Eng 17:073001
40. Tůma K, Stupkiewicz S, Petryk H (2018) Rate-independent dissipation in phase-field modelling of displacive transformations. J Mech Phys Solids 114:117–142
41. Forest S (2009) Micromorphic approach for gradient elasticity, viscoplasticity, and damage. J Eng Mech 135:117–131
42. Rezaee-Hajidehi M, Stupkiewicz S (2021) Micromorphic approach to phase-field modeling of multivariant martensitic transformation with rate-independent dissipation effects. Int J Solids Struct 222:111027
43. Miehe C (2011) A multi-field incremental variational framework for gradient-extended standard dissipative solids. J Mech Phys Solids 59:898-923
44. Hildebrand FE, Miehe C (2012) A phase field model for the formation and evolution of martensitic laminate microstructure at finite strains. Philos Mag 92:4250–4290
45. Bartels A, Mosler J (2017) Efficient variational constitutive updates for Allen-Cahn-type phase field theory coupled to continuum mechanics. Comput Methods Appl Mech Eng 317:55–83
46. Rockafellar RT (1970) Convex analysis. Princeton University Press, Princeton, New Jersey
47. Steinmann P, Stein E (1996) On the numerical treatment and analysis of finite deformation ductile single crystal plasticity. Comput Methods Appl Mech Eng 129:235–254
48. Alart P, Curnier A (1991) A mixed formulation for frictional contact problems prone to Newton like solution methods. Comput Methods Appl Mech Eng 92:353–375
49. Petryk H (2020) A quasi-extremal energy principle for non-potential problems in rate-independent plasticity. J Mech Phys Solids 136:103691
50. Stupkiewicz S, Petryk H (2013) A robust model of pseudoelasticity in shape memory alloys. Int J Num Methods Eng 93:747–769
51. Michaleris P, Tortorelli DA, Vidal CA (1994) Tangent operators and design sensitivity formulations for transient non-linear coupled problems with applications to elastoplasticity. Int J Num Methods Eng 37:2471–2499
52. Korelc J (2009) Automation of primal and sensitivity analysis of transient coupled problems. Comput Mech 44:631–649
53. Korelc J, Wriggers P (2016) Automation of finite element methods. Springer, Cham
54. de Souza Neto EA, Perić D, Dutko M, Owen DRJ (1996) Design of simple low order finite elements for large strain analysis of nearly incompressible solids. Int J Solids Struct 33:3277–3296
55. Rezaee Hajidehi M, Stupkiewicz S (2018) Gradient-enhanced model and its micromorphic regularization for simulation of Lüders-like bands in shape memory alloys. Int J Solids Struct 135:208–218